CD-MPM: Continuum Damage Material Point Methods for Dynamic Fracture Animation

JOSHUAH WOLPER, University of Pennsylvania
YU FANG, University of Pennsylvania
MINCHEN LI, University of Pennsylvania
JIECONG LU, University of Pennsylvania
MING GAO, University of Pennsylvania
CHENFANFU JIANG, University of Pennsylvania

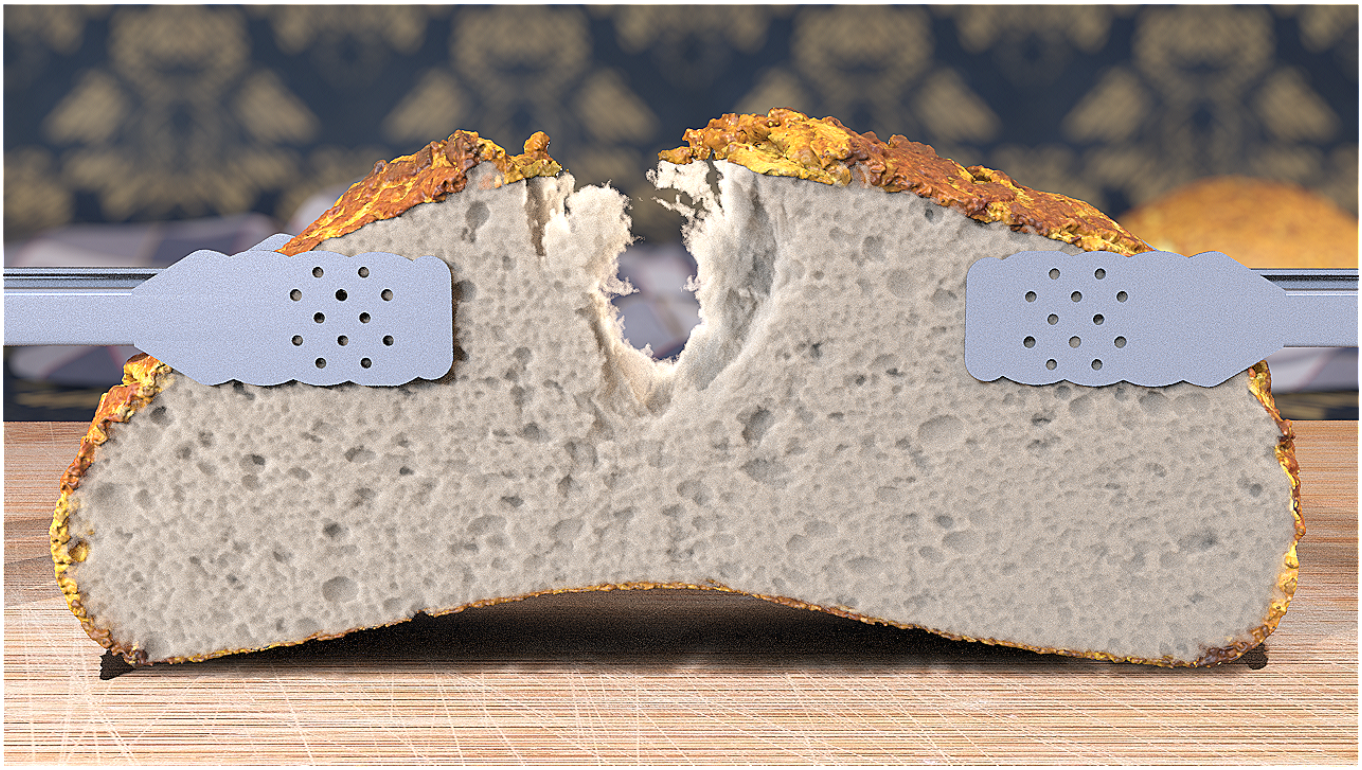

Fig. 1. **Breaking Bread.** We tear a slice of bread with more than 11 million PFF-MPM particles, revealing intricate fracture patterns and natural dynamics.

We present two new approaches for animating dynamic fracture involving large elastoplastic deformation. In contrast to traditional mesh-based techniques, where sharp discontinuity is introduced to split the continuum at crack surfaces, our methods are based on Continuum Damage Mechanics (CDM) with a variational energy-based formulation for crack evolution. Our first approach formulates the resulting dynamic material damage evolution with a Ginzburg-Landau type phase-field equation and discretizes it with the Material Point Method (MPM), resulting in a coupled momentum/damage solver rooted in phase field fracture: PFF-MPM. Although our PFF-MPM approach achieves convincing fracture with or without plasticity, we also introduce a return mapping algorithm that can be analytically solved for a wide range of general non-associated plasticity models, achieving more than two times speedup over traditional iterative approaches. To demonstrate the efficacy of the algorithm, we also develop a Non-Associated Cam-Clay (NACC) plasticity model with a novel fracture-friendly hardening scheme. Our NACC plasticity paired with traditional MPM composes a second approach to dynamic fracture, as it produces a breadth of organic, brittle

Authors' addresses: Joshuah Wolper, University of Pennsylvania; Yu Fang, University of Pennsylvania; Minchen Li, University of Pennsylvania; Jiecong Lu, University of Pennsylvania; Ming Gao, University of Pennsylvania; Chenfanfu Jiang, University of Pennsylvania.

0730-0301/2019/7-ART119 $15.00
https://doi.org/10.1145/3306346.3322949

material fracture effects on its own. Though NACC and PFF can be combined, we focus on exploring their material effects separately. Both methods can be easily integrated into any existing MPM solver, enabling the simulation of various fracturing materials with extremely high visual fidelity while requiring little additional computational overhead.

CCS Concepts: • **Computing methodologies** → **Physical simulation**.

Additional Key Words and Phrases: Material Point Method (MPM), phase-field, material damage, ductile fracture

ACM Reference Format:
Joshuah Wolper, Yu Fang, Minchen Li, Jiecong Lu, Ming Gao, and Chenfanfu Jiang. 2019. CD-MPM: Continuum Damage Material Point Methods for Dynamic Fracture Animation. *ACM Trans. Graph.* 38, 4, Article 119 (July 2019), 15 pages. https://doi.org/10.1145/3306346.3322949

1 INTRODUCTION

We often have to rush through dinner and a movie, but slow down and look closer as countless unseen illustrations of material fracture swim into focus. Warm, fresh bread is torn as hundreds of bubbles warp and tear, leaving intricate fissures. A saltine falls and shatters as fine debris puffs up, lightly spattering the ground. Later, in the newest action movie, a car smashes through a fence, leaving a twisted metal exit. In a final chase, fruit stands explode in rainbows of supple chunks as a fine mist spreads on the breeze.

Dynamic fracture is ubiquitous to everyday life, but the mechanics underlying these intricate material changes are anything but simple. In computer graphics, fracture simulation requires methods for large-scale topological changes at varying rates, as well as robust procedures for tracking the evolving crack fronts. Existing work takes on a variety of approaches to fracture depending on the application: real time applications prefer procedural [Neff and Fiume 1999] or example-based methods [Mould 2005], while offline applications typically adopt physically-based simulation. These physics-based approaches further deviate in their choice of discretization of the governing equations: finite element methods (FEMs) were among the first to be successful [O'Brien et al. 2002; O'Brien and Hodgins 1999], boundary element methods (BEMs) are recently gaining traction [Da et al. 2016; Hahn and Wojtan 2015, 2016], and meshless methods showed success for large topology change of solids early on [Pauly et al. 2005] and are on the rise with the growing versatility and popularity of the Material Point Method (MPM) [Sulsky et al. 1995]. Though they show great success, mesh-based methods require computationally intensive re-meshing routines or complex algorithms like VNA and XFEM [Koschier et al. 2017; Molino et al. 2005] and BEMs in particular have not yet been successfully applied to ductile fracture. Conversely, meshless methods such as MPM show great promise due to automatic support for arbitrarily large topological changes, natural collision handling, and a wide variety of successfully simulated continuum materials.

Despite the breadth of discretization approaches, most fracture methods in computer graphics have focused on fracture mechanics (FM) since it is a natural pairing with finite element fracture. In FM, cracks are discretely represented and modeled originally by the separation of nodal points in a mesh [Ngo and Scordelis 1967]; however, this introduced strong mesh dependency, and as such, many mesh-refinement and remeshing techniques were developed.

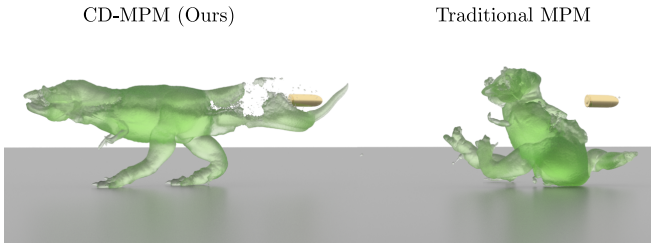

Fig. 2. **Jello T-Rex.** A jello T-rex is shot at high speed with a bullet; here we compare our PFF-MPM with traditional MPM to show that visually plausible fracture is unattainable with the latter.

More recently, the extended finite element method (XFEM) obviates remeshing by instead tracking the crack by iteratively enhancing mesh node DOFs [Belytschko and Black 1999; Koschier et al. 2017; Moës et al. 1999; Sukumar et al. 2000].

Though FM has proven a strong method for visually plausible results in graphics, another approach to fracture saw significant exploration concurrently with FM: continuum damage mechanics (CDM) [Rashid 1968]. In contrast with FM, CDM uses a *smeared crack* approach in which the cracked material is assumed to remain a continuum and, instead, the mechanical properties are weakened based on the evolving stresses and strains of the material to account for the effects of fracture. Within CDM, damage can be modeled either locally, such as through computing the ratio of a defined maximal stress and the current local stress [Cervera and Chiumenti 2006], or non-locally such as through tracking a scalar field of damage variables evolving over time, known as phase-field fracture (PFF) [Borden et al. 2016, 2012]. Local CDM has the advantage of predicting the crack tip more accurately; however, it struggles to produce all modes of fracture and, when paired with meshed methods like FEM, the direction and speed of the crack evolution depends on mesh direction and resolution [Grassl and Jirásek 2004]; conversely, non-local CDM still predicts the crack tip and has the benefit of capturing all modes of fracture while producing mesh invariant crack propagation. As such, we choose to pair the non-local PFF with MPM based on its robust capturing of all fracture modes and

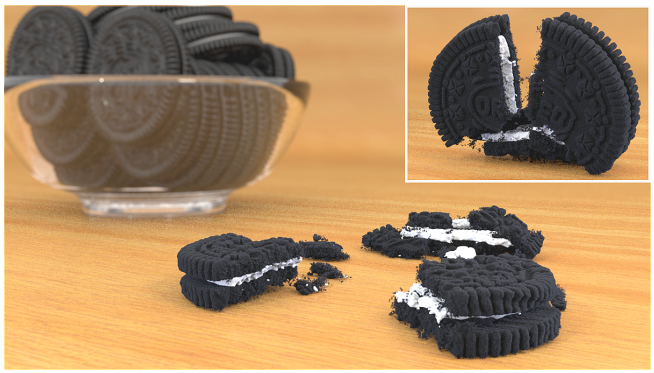

Fig. 3. **Cookie Smash.** Our NACC plasticity naturally captures brittle fracture behavior of mixed materials when a cookie is dropped onto the ground.

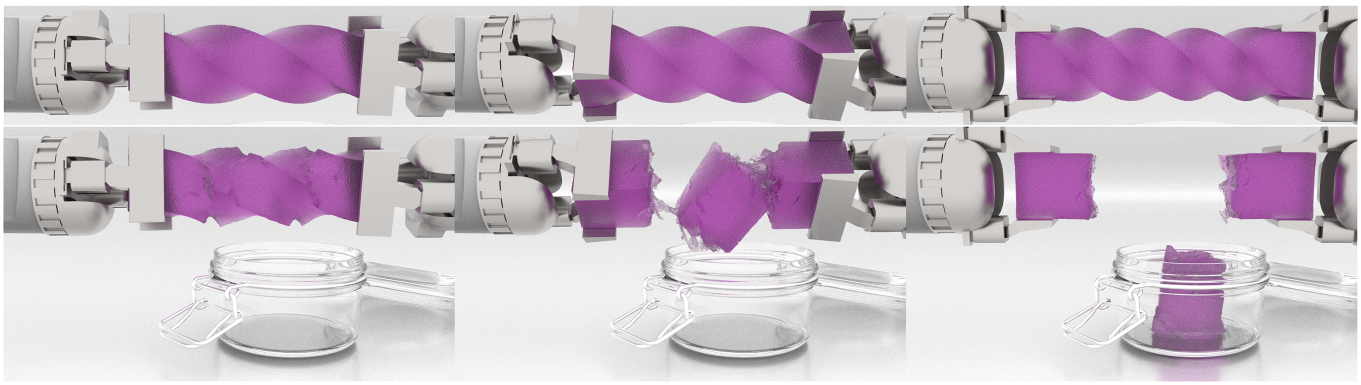

Fig. 4. **Bar Twist.** An elastic bar with $7.79M$ particles is twisted with traditional MPM (top) and PFF-MPM (bottom) to show the dynamic fracture achievable.

resolution invariance, and for how naturally a scalar field evolution technique aligns with the grid-based computations of MPM.

While MPM is a natural choice for a meshless fracture discretization, it historically suffers from difficulty handling discontinuities appearing in the material. This was recently addressed with the compatible particle in cell algorithm (CPIC) for material cutting in MPM; however, CPIC does not generalize to fracture and cannot model branching cracks [Hu et al. 2018]. Fortunately, PFF allows for the continuum to be treated as a whole throughout simulation, and fracture occurs strictly through the degradation of stress over time based on the evolving phase-field values. This formulation allows us to solve the systems for momentum and damage in a staggered manner, giving a low-overhead augmentation to standard MPM that allows for a wide variety of material fracture effects: PFF-MPM.

In addition to our PFF-MPM approach to material fracture, we are also inspired by recent techniques that degrade elastic stress through their treatments of plasticity [Pradhana et al. 2017; Stomakhin et al. 2013; Yue et al. 2015] and expand upon the Cohesive Cam-Clay plasticity model of Gaume et al. [2018] to present a non-associated and volume preserving plasticity model that enables materials to dynamically fracture when paired with traditional MPM: Non-Associated Cam-Clay (NACC). Though PFF-MPM and the NACC plasticity model can be used together, they each stand as their own unique approach to dynamically animating fracture effects, and as such, we predominantly explore them individually (all demos run with either PFF-MPM or NACC plasticity unless otherwise noted).

1.1 Contributions

Our major contributions within CD-MPM lie in the development of PFF-MPM, an augmented MPM adopting continuum damage mechanics and phase-field theory for dynamic brittle and ductile fracture. We formulate crack propagation as a variational energy minimization problem through representing the damage state of the material with continuous phase-field variables. By proposing a novel incremental potential for backward Euler integration of the phase-field, our governing equation resembles a Ginzburg-Landau type equation widely adopted in structural engineering. We develop a novel weak form discretization of the phase-field evolution equation using MPM. Similar to the heat equation, the phase-field discretization results in a symmetric positive-definite linear system, which is efficiently solvable together with the momentum.

We additionally present as part of CD-MPM a backward Euler based finite strain plasticity scheme that enables a highly efficient analytic return mapping for a wide range of general non-associated (plastic volume preserving) plasticity models. In addition to the widely adopted von Mises and Drucker-Prager plasticity, we introduce a Non-Associated Cam-Clay (NACC) model with a novel strain hardening scheme for capturing a breadth of material fracture behaviors with superior performance and ease of implementation. Overall, our phase-field solver and new constitutive models can be easily integrated into any existing MPM framework with minor modifications and each presents a novel approach to dynamic fracture animation. We demonstrate the efficacy of each method by simulating various elastoplastic materials undergoing fracture.

2 RELATED WORK

2.1 Fracture Simulation

Since Terzopoulos and Fleischer's [1988] seminal work on viscoelastic fracture in graphics, research has taken a variety of approaches to simulating this notoriously difficult physical phenomenon. Within graphics, these methods range from those seeking to simulate the physical systems behind fracture mechanics as we understand them, to approximation approaches formulated to obviate physics and accuracy in favor of speed and visual plausibility. However, these latter approaches are limited in three ways: they are not physically accurate, can require lengthy data acquisition, and lack successful simulation of dynamic ductile fracture (historically, these exclusively focus on quasistatic or dynamic brittle fracture). Though these are still widely explored, physically based methods now comprise the bulk of fracture simulation approaches. Mass-spring models were among the first and represented continuum materials as point masses connected by springs with stress-based yield thresholds [Aoki et al. 2004; Hirota et al. 1998, 2000; Norton et al. 1991]. However, these models are severely limited: sudden spring removal causes notable visual artifacts [Norton et al. 1991]; shearing and bending are not directly handled by spring systems and require further engineering [Hirota et al. 1998; Norton et al. 1991]. Most notably, the exact fracture surfaces themselves are not known but

Fig. 5. **Watermelon Smash.** A mixed material watermelon is smashed on the ground illustrating dynamic, organic fracture and debris spray using NACC.

are instead approximated based on the mass spring configuration and, as such, crack visualization is not only limited by the configuration and resolution, but also often require computationally intensive tetrahedral marching algorithms [Hirota et al. 1998, 2000]. Contrary to mass-spring methods, more recent physical approaches alleviate some of these problems through the use of modal analysis to simulate real-time brittle fracture [Glondu et al. 2013, 2014], moving cellular automata (MCA) to discretize the fracturing material [Ning et al. 2013], or even careful conversion of fracture energy into kinematic energy during rigid body simulation [Li et al. 2018]. However, these newer, more complex approaches have their own limitations: modal analysis is limited to brittle fracture, and the use of MCA brings with it intensive computational costs.

While these other approaches have gained some recent traction, finite element methods (FEMs) for simulating fracture have been shown to be among the most successful for brittle [Bao et al. 2007; Müller and Gross 2004; O'Brien and Hodgins 1999], ductile [Bao et al. 2007; Müller and Gross 2004; O'Brien et al. 2002], and thin shell [Busaryev et al. 2013] materials; successful FEMs achieve this by representing materials as tetrahedral meshes with elements that are individually deformed and cut during simulation. However, FEMs pose difficult geometric and computational challenges, including remeshing near cracks, representing topological discontinuities, and mesh cutting; as such, most subsequent works in FEM fracture address these challenges. Numerous remeshing approaches have been explored ranging from dynamic local mesh refinement [Wicke et al. 2010], to remeshing based on gradient descent flow [Chen et al. 2014], to remeshing for thin sheet fracture [Pfaff et al. 2014]. Topological discontinuities are often addressed through augmenting FEM with new schemes such as Discontinuous Galerkin FEM (DGFEM) [Kaufmann et al. 2008] or the level set method used to minimize Griffith's energy for ductile fracture in Hegemann et al. [2013].

Fortunately, FEM mesh cutting improved greatly with the virtual node algorithm (VNA) [Molino et al. 2005] which duplicates elements that intersect with crack topology rather than splitting them. Though limited at first, VNA has been expanded to allow for cutting at resolutions lower than mesh resolution [Sifakis et al. 2007] and to robustly handle degenerate intersections [Wang et al. 2014]. Most recently, eXtended FEM (XFEM), a remesh-free cutting algorithm, was shown to better conserve mass and preserve material stiffness of simulated materials [Koschier et al. 2017]. Despite these recent advances in remeshing and cutting, VNA and XFEM pose additional complexities such as floating point arithmetic in degenerate configurations and self-collision on their embedded meshes.

While FEMs focus on processing fracture with a volume discretization, boundary element methods (BEMs) simply discretize fracture mechanics across material surfaces. First introduced in graphics by James and Pai [1999] for the formulation of elastostatic deformable objects, BEMs have more recently been paired with linear elastic fracture mechanics to successfully simulate brittle fracture while utilizing Lagrangian crack fronts [Hahn and Wojtan 2015] and local triangle mesh operations [Zhu et al. 2015] for the tracking of highly detailed cracks. Further study has been devoted to fast approximations for BEM brittle fracture to mitigate high computational overhead [Hahn and Wojtan 2016]. Though very successful for brittle materials, BEMs have not yet produced successful ductile fracture nor have they been paired with CDM to track fracture.

Though most recent study has focused on FEMs, meshless methods have gained great traction recently with the Material Point Method (MPM) [Sulsky et al. 1995]. MPM is a powerful choice for simulating a breadth of materials and behaviors, going so far as to enter the realm of VFX in major motion pictures [Stomakhin et al. 2013]. Meshless fracture approaches represent materials as sets of particle masses with no connectivity and, as such, obviate the complex remeshing and cutting procedures of FEMs. Early approaches to meshless fracture simulation include element-free Galerkin (EFG) [Belytschko et al. 1995; Lu et al. 1995; Sukumar et al. 1997] which requires node-visibility algorithms; CRAMP which augments MPM to track cracks with massless particles and requires grid nodes to have multiple velocity fields near crack geometry [Nairn 2003]; Moving Least Squares with volume sampling [Müller et al. 2004]; and, expanding on the latter, resampling during crack propagation and adapting the shape functions dynamically [Pauly et al. 2005] to simulate both brittle and ductile fracture. More recent works incorporate clustered shape matching for ductile fracture [Jones et al. 2016]; the local Petrov-Galerkin method (MLPG) to avoid lengthy neighbor searches [Liu et al. 2011]; and, similarly, smoothed particle hydrodynamics (SPH) has shown success in simulating brittle fracture [Chen et al. 2013]. Though successful, some of these methods produce notable directional artifacts due to element removal.

Most recently, MPM has shown great potential for fracture simulation due to its automatic handling of extreme topological changes (including material split and merge, which are both difficult for FEM) as well as its lack of boundary difficulties typically associated

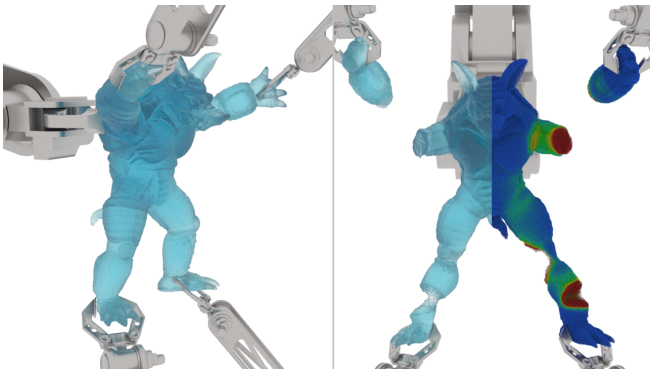

Fig. 6. **Armadillo Stretch.** A jello armadillo's limbs are ripped off to illustrate the intricate fractures achievable with PFF-MPM; phase-field values are shown in world space to show damaged regions.

with kernel techniques like SPH. Typically, MPM alone is incapable of modeling sharp discontinuities, and past approaches to MPM fracture have relied on pre-fracture to handle this [Wretborn et al. 2017]. However, Hu et al. [2018] recently introduced the Compatible Particle-in-Cell (CPIC) algorithm, which allows these discontinuities and achieves dynamic material cutting with sharp boundaries.

Though CPIC with MPM shows great potential for dealing with sharp discontinuities, it does not in any way seek to simulate dynamic fracture behaviors. However, strong examples of MPM fracture have been explored and focus on the viscoplastic models intrinsic to fracture in geological materials (soil and rocks) and complex viscous fluids (such as foam). These works explore fracture animation through the lens of plasticity weakening. Stomakhin et al. [2013] modeled snow fracture by decreasing elastic stiffness as expansive plastic strain accumulates. Pradhana et al. [2017] used a saturation-dependent cohesion parameter in the Drucker-Prager plasticity model to support wet sand breakage. Yue et al. [2015] modeled foam tearing through introducing weak particles during plastic yielding. The Non-Associated Cam-Clay (NACC) model we propose in this paper lies in the same category. Independent from whether a phase-field damage evolution is active, our model captures many fracture phenomena due to localized shear and tensile deformation.

2.2 Continuum Damage Mechanics and Phase-Field Fracture

Fracture theory has two main numerical modeling approaches: discontinuous methods that allow fracture surfaces to be represented in the displacement field as discontinuities, and continuous methods that model the displacement as being continuous everywhere (here, fracture occurs by gradually decreasing stresses to model degradation). Discontinuous methods are typically composed of either linear elastic fracture mechanics, pioneered by Griffith [1921] and Irwin [1957], or the cohesive zone model [Barenblatt 1962]. The most widely used continuous method is continuum damage mechanics (CDM) which seeks to evolve some damage variable throughout simulation to model the evolution of fracture [Kachanov 1999]. However, two emergent continuous methods have shown success since their introduction: peridynamics (PD) [He et al. 2018; Levine et al. 2014; Silling 2000; Silling and Askari 2005], and phase-field fracture (PFF) [Aranson et al. 2000; Bourdin et al. 2000; Francfort and Marigo 1998]. In PD models, the usual partial differential equations are replaced with integral ones such that derivative computation is avoided, and recently, combining PFF for brittle fracture with the integral framework of PD showed great success [Roy et al. 2017], as the two combined achieved effects unattainable by one or the other model (such as the splitting of individual particles).

Though PD models have shown success, PFF methods are currently under deeper exploration within the engineering community. For brittle fracture, PFFs have gained traction with a more straightforward reformulation that has shown to be more accessible to the engineering community [Miehe et al. 2010b]. Recent PFF works seek to design better degradation functions and use the length scale parameter l_0 in order to better model the transition region of the damaged material over time [Wu 2017, 2018]. Ductile fracture within the framework of PFF has also garnered interest and shown success for quasistatic configurations and finite strains by relying on a multiplicative decomposition of the stress into its elastic and plastic parts as well as an additive decomposition of the constitutive models into tensile and volumetric components [Ambati et al. 2016; Borden et al. 2016; Miehe et al. 2015]. Most recently, geologically-inspired work has explored whether return mapping routines should include plastic degradation functions since they may break assumptions about which stress is used to evaluate the yield condition [Choo and Sun 2018]. Though PFF is still nascent, it has clearly shown success within the engineering community at predicting crack initiation and propagation, and as such, we propose to explore its use within graphics for both its high visual fidelity and predictive accuracy.

2.3 Material Point Method

MPM is a generalization of the hybrid Fluid Implicit Particle (FLIP) method [Brackbill and Ruppel 1986; Zhu and Bridson 2005] from computational fluid dynamics to solid mechanics. Since its introduction by Sulsky et al. [1994; 1995], MPM has proven to be a promising

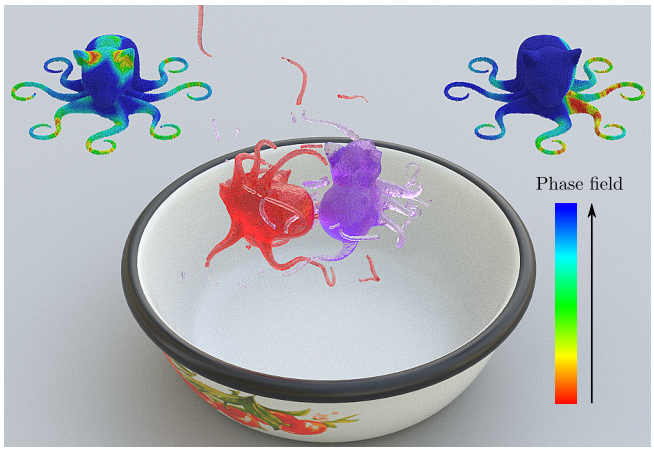

Fig. 7. **Octocat Collision.** Two fragile-armed octocats' tentacles break as they collide mid-air using PFF-MPM; material space phase-field propagation is visualized to show where damage occurs.

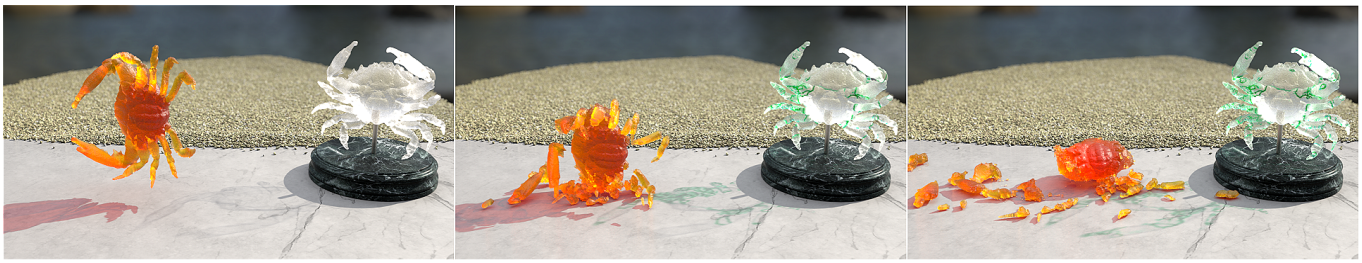

Fig. 8. **Candy Crab.** The brittle fracture of fallen candy is shown propagating in material space by visualizing the NACC hardening parameter, α, in green.

discretization choice for simulating many solid and fluid materials. In the field of physics-based animation, the existing works include snow [Stomakhin et al. 2013], foam [Ram et al. 2015; Yue et al. 2015], sand [Daviet and Bertails-Descoubes 2016; Klár et al. 2016; Yue et al. 2018], cloth [Fei et al. 2018; Guo et al. 2018; Jiang et al. 2017] and solid-fluid mixtures [Gao et al. 2018a; Pradhana et al. 2017; Stomakhin et al. 2014]. Echoing recent works, our treatment of the damage state is similar to how Gao et al. [2018b] treats heat conduction, since we also discretize the governing parabolic PDE using Moving Least Squares MPM [Hu et al. 2018].

2.4 Phase-Field Modeling

Phase-field modeling began as a popular approach in computational physics for simulating complex multi-phase effects like solidification; however, its ability to continuously model an interface between different material phases has also proven useful in computer graphics for simulating the formation of ice crystals by pairing phase-field with diffusion limited aggregation [Kim et al. 2004] and the mixing of fluids [He et al. 2015]. Similarly, Yang et al. [2015] achieved fast multiphase fluid simulation by evolving mass concentration variables using the Cahn-Hilliard equation [Cahn and Hilliard 1958]. Most recently, Yang et al. [2017] attained complex multi-material simulation, expanding on this work by introducing a phase proportion variable evolved over time with the Allen-Cahn equation [Allen and Cahn 1972], which is quite similar in formulation to our damage evolution governing equation.

3 GOVERNING EQUATIONS

3.1 Variational Formulation

For an elastic body with material space Ω^0 and deformed space Ω^t under deformation map $\boldsymbol{x} = \phi(\boldsymbol{X}, t)$ where $\boldsymbol{x}$ and $\boldsymbol{X}$ are world and material coordinates respectively, Griffith's theory of fracture [Griffith and Eng 1921] defines the total free energy to be the summation of the elastic potential and the released energy at crack surfaces:

$$\mathcal{E}(\boldsymbol{F}, \mathcal{T}) = \int_{\Omega^0} \hat{\Psi}(\boldsymbol{F}) d\boldsymbol{X} + \int_{\mathcal{T}} \mathcal{G} d\boldsymbol{X}, \tag{1}$$

where $\boldsymbol{F} = \frac{\partial \phi}{\partial \boldsymbol{X}}$ is the deformation gradient, $\hat{\Psi}(\boldsymbol{F})$ is a degraded (damaged) finite-strain hyperelastic energy density function (see §3.2), $\mathcal{T}$ denotes the *internal* discontinuous boundary due to fracture, and $\mathcal{G}$ is the critical energy release rate (also called fracture toughness) of the material, denoting the energy released when a unit area fractures. In a quasistatic case, solving the minimization of $\mathcal{E}$ predicts the crack propagation [Francfort and Marigo 1998] under given external loads. In computer graphics, Hegemann et al. [2013] used a level set to separate the continuum into a healthy region and a damaged region (with interface $\mathcal{T}$). This approach requires frequent re-initialization of a signed distance function and cannot resolve non-manifold topology without more complex representation [Mitchell et al. 2015]. Thus, we instead use a phase-field approximation to the surface integral [Bourdin et al. 2008]:

$$\int_{\mathcal{T}} \mathcal{G} d\boldsymbol{X} \approx \int_{\Omega^0} \left(\frac{(c-1)^2}{4 l_0} + l_0 |\nabla^{\boldsymbol{X}} c|^2 \right) \mathcal{G} d\boldsymbol{X}, \tag{2}$$

where l_0 is a discretization dependent length scale parameter ($l_0 \to 0$ causes the volume integral to converge to the surface integral), $c(\boldsymbol{X}, t) \in [0, 1]$ is the smooth phase-field throughout the continuum material, where $c = 1$ corresponds to healthy material and $c = 0$ to fully damaged material. We found that for MPM discretization, a length scale of $l_0 = 0.5\Delta x$ was sufficient for most of our demos.

3.2 Elasticity Degradation

Supposing the traditional hyperelastic energy density Ψ^E can be additively decomposed into a tensile contribution $\Psi^+(\boldsymbol{F})$ and a compressive contribution $\Psi^-(\boldsymbol{F})$, it is common in phase-field fracture theory [Amor et al. 2009; Miehe et al. 2010a,b] to degrade the tensile part with a monotonic degradation function $g(c)$ so that material separation is permitted along cracked regions. Specifically,

$$\hat{\Psi}(\boldsymbol{F}) = g(c)\Psi^+(\boldsymbol{F}) + \Psi^-(\boldsymbol{F}), \tag{3}$$

where $g(c) = (1 - r)c^2 + r$ is chosen to be a quadratic function for simplicity. Setting $r = 0.001$ in all of our examples allows a tiny residual tensile stress even for fully damaged regions. This avoids the potential unbounded growth of the deformation gradient for a fully damaged material and the ensuing floating point overflow.

Combining the above, the free energy functional can be written as $\mathcal{E}(\boldsymbol{F}, c) = \int_{\Omega^0} \Psi(\boldsymbol{F}, c) d\boldsymbol{X}$, where

$$\Psi(\boldsymbol{F}, c) = g(c)\Psi^+(\boldsymbol{F}) + \Psi^-(\boldsymbol{F}) + \left(\frac{(c-1)^2}{4 l_0} + l_0 |\nabla^{\boldsymbol{X}} c|^2 \right) \mathcal{G} \tag{4}$$

is the free energy density function accounting for the balance between elasticity degradation and energy release. See §5 and Fig. 14 to visualize this degradation concept for our elasticity.

3.3 Momentum Conservation

Here we move from the quasistatic setting into strongly nonlinear dynamics problems. We focus on the response of hyper-elastoplastic

Fig. 9. **Smashing Pumpkins.** Two jack'o'lanterns collide using NACC plasticity to achieve complex, organic fractures and debris spread; NACC α is visualized in material space at right to better visualize crack propagation.

solids, where the backward Euler time integration from t^n to t^{n+1} can be recast into a variational problem [Radovitzky and Ortiz 1999] minimizing an incremental potential. This is ideal, as approaches with optimization-based integrators have shown great success for efficient dynamics computations in computer graphics [Bouaziz et al. 2014; Liu et al. 2013, 2017; Narain et al. 2016; Wang and Yang 2016]. For our degraded hyperelastic object, the Lagrangian momentum conservation from t^n to t^{n+1} is given by:

$$\frac{R}{\Delta t^2}\phi^{n+1} - \nabla^{\boldsymbol{X}} \cdot \boldsymbol{P}^{n+1} = \boldsymbol{f}^{\text{ext}} + \frac{R}{\Delta t^2}(\phi^n + \Delta t \boldsymbol{V}^n), \tag{5}$$

where R is density, $\boldsymbol{P}^{n+1} = \frac{\partial \Psi}{\partial \boldsymbol{F}}(\boldsymbol{F}^{n+1})$ is the first Piola-Kirchhoff stress (see supplemental document [Wolper et al. 2019]). Note that with implicit Euler, we have $\phi^{n+1} = \phi^n + \Delta t \boldsymbol{V}^{n+1}$, which also allows us to reformulate Eqn. (5) in terms of velocities. Note that our derivation has assumed pure hyperelasticity since the implicit treatment of plasticity cannot be easily formulated as a minimization problem [Klár et al. 2016]. For plastic materials, we follow Jiang et al. [2016] and treat the plastic flow explicitly through a return mapping of the elastic deformation gradient at the end of each time step. The discretization of Eq. 5 can be accomplished with a slightly modified version of standard MPM as detailed in §4.1.

3.4 Phase-Field Evolution

In CDM, there are different strategies for evolving the damage state. In this section, we first introduce a simple, yet problematic damage evolution approach based on local damage mechanics. Then, we propose a novel incremental potential energy function for coupled phase-field and deformation evolution (deformation and damage affect one another). We show that our incremental potential leads to a Ginzburg-Landau type phase-field evolution equation that is consistent with existing literature on dynamic phase-field theory.

3.4.1 Local Damage Mechanics. Local damage mechanics assumes the damage state of each material point is only locally dependent on its own stress history. One of the most simplistic models of this kind is the linear strain-softening Rankine damage model [Cervera and Chiumenti 2006; Homel and Herbold 2017], where the material damage is linearly related to the maximum eigenvalue of the Cauchy stress, σ. If the principal stress is σ_M and the failure stress threshold is σ_f, then whenever $\sigma_M > \sigma_f$, the phase-field is updated as $c^{n+1} = \min(c^n, 1 - H_s(1 - \frac{\sigma_M}{\sigma_f}))$, where H_s is an empirical parameter controlling the brittleness. Although such local damage models are simple and efficient, they tend to cause undesired artifacts even on simple examples. Moreover, the crack propagation produced by local models has strong mesh direction and resolution dependency [Grassl and Jirásek 2004], which severely decreases the efficacy of offline simulation, since a satisfactory behavior at low resolution likely does not persist at high resolution. We experimentally compare local CDM to PFF-MPM in [Wolper et al. 2019].

3.4.2 Parabolic Phase-field Evolution. To avoid the problems with local damage mechanics, we target a phase-field evolution rule that is constructed using Ginzburg-Landau theory [Landau and Lifshitz 1971] following general thermodynamics and kinetics. By augmenting the traditional incremental potential with additional inertia terms related to c (see [Wolper et al. 2019] for more details), the Euler-Lagrangian equation for $c^{n+1}(\boldsymbol{X})$ reveals:

$$\left(\frac{4l_0 M_c(1-r)\Psi^+}{\mathcal{G}} + M_c + \frac{1}{\Delta t}\right)c^{n+1} - (4l_0^2 M_c)\nabla^2 c^{n+1} = r, \tag{6}$$

where $r = M_c + (c^n/\Delta t)$ is the right hand side scalar, $M_c = \mathcal{G}/(2R_c l_0)$ is a material parameter, and ∇^2 is the Laplace operator with respect

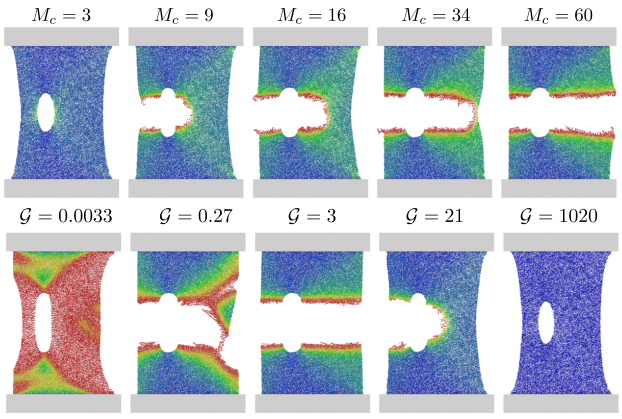

Fig. 10. **PFF-MPM Parameters.** The breadth of fracture behavior attainable through phase-field parameters is illustrated here, showcasing the effects of changing the energy release rate, $\mathcal{G}$, and mobility constant, M_c.

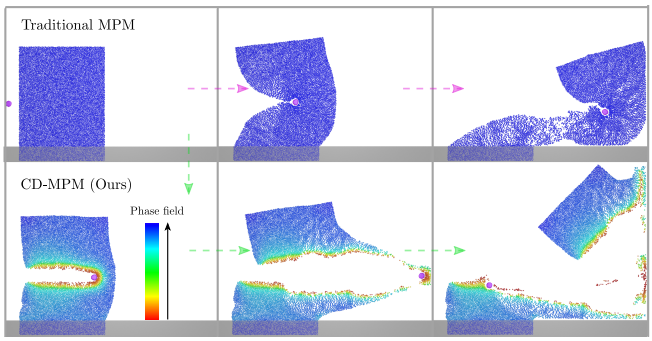

Fig. 11. **Shooting Cake.** A cake-like material is shot with an elastic bullet and simulated with both PFF-MPM and NACC plasticity; we compare against traditional MPM to show the efficacy of our CD-MPM methods.

to $\boldsymbol{X}$ (see Fig. 10 to see the impact of M_c and $\mathcal{G}$). Note that Yang et al. [2017] also used a similar Allen-Cahn equation to evolve phase-field variables for their unified multi-phase multi-material simulations. Further, we need to impose the crack irreversibility condition $\mathcal{T}^n \subseteq \mathcal{T}^{n+1}$. This can be done by replacing Ψ^+ in Eqn. (6) with its history dependent version $\Psi^{\mathcal{H}}$, which is only updated when a new maximum Ψ^+ is achieved at the corresponding material point. In Fig. 11 we show the efficacy of our PFF-MPM formulation and its successful pairing with NACC plasticity.

4 PFF-MPM SPATIAL DISCRETIZATION

Here we discuss the MPM discretization of Eqn. (5) and Eqn. (6). MPM uses meshless quadrature particles to carry Lagrangian physical quantities, and a background grid to evaluate spatial derivatives. A distinct feature of MPM, compared to FEM, is the view of Updated Lagrangian (UL) in contrast to the view of Full Lagrangian (FL). With UL, MPM treats the time t^n configuration as the material space and seeks to approximate the deformation map from t^n to t^{n+1}. As such, spatial derivatives with respect to $\boldsymbol{X} \in \Omega^0$ in previous sections can be modified into derivatives with respect to $\boldsymbol{x}^n \in \Omega^n$. Note that we use the same symbol c to denote Eulerian and Lagrangian phase-field quantities, with the understanding that all Lagrangian quantities are pushed forward into their Eulerian counterparts to enable an MPM discretization. We list for clarity which quantities are tracked per particle, which are transferred to the grid, and which are constant simulation parameters in Table 1.

4.1 Newtonian Dynamics

The momentum equation is solved following standard MPM, with the exception that the stress is influenced by the phase-field. Here we list the main steps (see [Jiang et al. 2016] and [Hu et al. 2018] for more details). We use subscripts p, q for particle quantities and i, j, k for grid node quantities. Superscript $n, n+1$ are for quantities at discrete time t^n and t^{n+1} where $\Delta t = t^{n+1} - t^n$.

(1) **Particles to grid.** Mass and momentum are transferred to the grid with APIC [Jiang et al. 2015]: $m_i^n = \sum_p m_p w_{ip}^n$ and $(m\boldsymbol{v})_i^n = \sum_p m_p w_{ip}^n \left(\boldsymbol{v}_p^n + \mathbf{C}_p^n(\boldsymbol{x}_i - \boldsymbol{x}_p^n)\right)$, where $\mathbf{C}_p^n$ is the APIC velocity gradient and w_{ip}^n is the quadratic B-spline interpolation weight between particle p and node i.

(2) **Grid update.** Grid velocity is updated with MLS-MPM forces $\boldsymbol{f}_i^* = -\sum_p V_p^0 w_{ip}^n M_p^{-1} \frac{\partial \Psi}{\partial \boldsymbol{F}}(\boldsymbol{F}_p^*, c_p^{n+1}) \boldsymbol{F}_p^{n\,T}(\boldsymbol{x}_i^n - \boldsymbol{x}_p^n)$, where V_p^0 is the original volume of particle p, $M_p^{-1} = \frac{4}{\Delta x^2}$ for a quadratic particle-grid kernel, $* = n$ or $n+1$ for symplectic Euler and implicit Euler respectively. For implicit integration, we further use the force differential in [Hu et al. 2018] to evaluate the action of the global stiffness matrix.

(3) **Grid to particles.** Particle velocities are updated with $\boldsymbol{v}_p^{n+1} = \sum_i \boldsymbol{v}_i^{n+1} w_{ip}^n$ followed by position advection. Velocity gradients are updated with $\mathbf{C}_p^{n+1} = M_p^{-1} \sum_i w_{ip}^n \boldsymbol{v}_i^{n+1} (\boldsymbol{x}_i^n - \boldsymbol{x}_p^n)^T$.

(4) **Strain update.** Particle deformation gradients are updated with MLS-MPM as $\boldsymbol{F}_p^{n+1} = (\boldsymbol{I} + \Delta t \mathbf{C}_p^{n+1}) \boldsymbol{F}_p^n$ and processed according to proper plasticity projection (§6).

Note that in step (2), the energy density function Ψ depends on the updated damage state c_p^{n+1} due to the elasticity degradation (§3.2).

Table 1. **Particle Quantities.** Here we list which quantities are tracked per particle, transferred to grid nodes, and constant throughout simulation.

Tracked Particle Quantities	m_p, x_p, v_p, APIC C_p, F_p, PFF c_p, NACC α_p
Transferred Grid Quantities	x_i, v_i, F_i, f_i, PFF c_i
Simulation Parameters	E, ν, PFF $(\mathcal{G}, M_c)$, NACC $(\alpha_0, \beta, \xi, M)$

4.2 Phase-Field Evolution

We develop a novel MPM-based discretization scheme for the phase-field governing Eqn. (6). Similarly to the velocities, the phase-field variable, c, advects with the MPM particles and needs to be transferred back and forth between the particles and the grid. We present in Fig. 12 a visualization of how we represent continuum cracks within this MPM discretization of phase-field evolution.

4.2.1 Phase-field Transfers. The phase-field is a physical intrinsic property of the object. The transfer from particles to grid is therefore

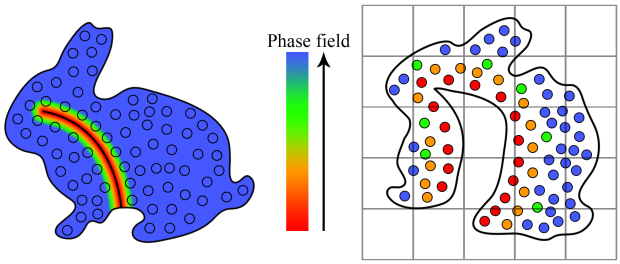

Fig. 12. **Continuum crack representation and discretization.** (Left) In material space, discontinuity is approximated with a continuous phase-field ranging from 0 to 1 while particle-based discretization uses finite-sized particles to track material attributes including phase; (Right) MPM uses particles to carry the phase-field in Eulerian world space while the phase-field evolution equation is discretized on a background grid in MPM.

similar to the velocity: $c_i^n = (\sum_p w_{ip}^n c_p^n)/(\sum_p w_{ip}^n)$. After solving for c_i^{n+1} on the grid, we transfer the phase-field back to particles as $c_p^{n+1} = \max(0, \min(c_p^n, c_p^n + \sum_i (c_i^{n+1} - c_i^n) w_{ip}^n))$. Note that we compare the new phase-field value against its current value to prevent any material healing. The phase-field is also explicitly restricted to the range $[0, 1]$ to eliminate accumulated noise from the FLIP-like transfer. We choose FLIP to avoid the numerical diffusion associated with PIC as this would lead to constant and uniform material degradation even when unloaded; furthermore, we leave the exploration of bound-preserving APIC/PolyPIC-style transfers for future work.

4.2.2 MLS Weak Form Discretization on the Grid. Starting with our backward Euler phase-field equation, Eqn. (6), we expand continuous quantities with the grid node-wise MLS shape function $\Theta_i(\boldsymbol{x})$ and its gradient $\nabla\Theta_i(\boldsymbol{x}_p) = M_p^{-1} w_{ip}^n (\boldsymbol{x}_i - \boldsymbol{x}_p^n)$ to achieve a symmetric positive definite linear system for the unknown c_i^{n+1} at grid nodes:

$$(\mathcal{M} + \boldsymbol{H})\mathbf{c} = \boldsymbol{r} \tag{7}$$

where $\mathbf{c}$ is the vector of all nodal unknowns,

$$\mathcal{M} = [\mathcal{M}_{ii}] = \sum_p V_p^n \left(\frac{4 l_0 M_c (1-r) \Psi_p^{\mathcal{H}}}{\mathcal{G}} + M_c + \frac{1}{\Delta t} \right) w_{ip}^n$$

is the diagonal lumped mass matrix (V_p^n is the current volume of p),

$$\boldsymbol{H} = \left[\boldsymbol{H}_{ij}\right] = \sum_p V_p^n (4 l_0^2 M_c)(\nabla\Theta_i(\boldsymbol{x}_p^n))^T (\nabla\Theta_j(\boldsymbol{x}_p^n))$$

is the MPM-based discrete Laplace operator, and

$$\boldsymbol{r} = [r_i] = \sum_p V_p^n (M_c + \frac{c_p^n}{\Delta t}) w_{ip}^n$$

is the corresponding right hand side (see [Wolper et al. 2019] for detailed derivation). We solve this system using conjugate gradient (CG). In practice, we found that the Jacobi preconditioner works well and no more than 4 CG iterations are usually required to reach near-roundoff accuracy. Note that the weak form based discretization naturally satisfies a Neumann boundary condition at the free surface and no special treatment is needed at collision object boundaries.

4.3 Staggered Integration

Although it is possible to couple the system solves for momentum and phase-field into one monolithic solve, this is typically prohibitively long. Instead, we choose a staggered integration scheme that involves two linear solves. In Fig. 13, we show two crucial relationships that arise in this staggered scheme: the particle deformation gradients, F_p^n, are used in the phase solve on the grid, and the results of the phase solve, c_p^{n+1}, are used in the grid force computation. We find that the phase solve is often adequately converged within a few CG iterations, and as such this contributes very little extra time to the overall algorithm (see Fig. 20). Note that multiple staggered iterations will be necessary for global convergence of the nonlinear problem; however, our experiments and the mechanics literature agree that 1-2 iterations is enough for close convergence and visually plausible results [Amor et al. 2009; Miehe et al. 2010a, 2015].

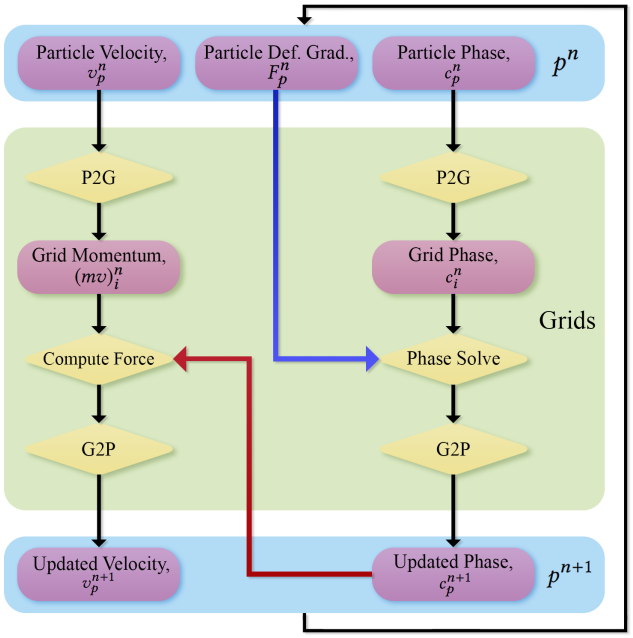

Fig. 13. **PFF-MPM Data Flow.** PFF-MPM utilizes a staggered integration scheme with two system solves on the grid: one for momentum and one for phase. The colored arrows show key details in our data flow; the blue shows the dependence of the grid phase solve on particle deformation gradients, and the red shows the use of the updated phases in the grid force update.

5 HYPERELASTICITY

In computer graphics, the hyperelastic energy density function is usually designed to simplify certain computations or to enable certain configurations. For example, the St. Venant-Kirchhoff energy with logarithmic strain was adopted for simplified derivation of plasticity [Klár et al. 2016], the fixed corotated energy was designed for robust treatment of inversion [Stomakhin et al. 2012], and the stable Neo-Hookean energy was designed for nice behaviors near the incompressibility limit [Smith et al. 2018]. For our purposes we want to achieve simple decomposition of the tensile and compressive contributions as well as simple derivation of plasticity return mapping (§6); as such, we adopt a variation of the Neo-Hookean model which was recently used by Yue et al. [2018]:

$$\Psi^E(\boldsymbol{F}) = \Psi^\mu(J^a \boldsymbol{F}) + \Psi^\kappa(\boldsymbol{F}), \tag{8}$$

$$\Psi^\mu(\boldsymbol{F}) = \frac{\mu}{2}(\mathrm{tr}(\boldsymbol{F}^T\boldsymbol{F}) - d) \text{ and } \Psi^\kappa(\boldsymbol{F}) = \frac{\kappa}{2}(\frac{J^2-1}{2} - \log J), \tag{9}$$

where Ψ^μ and Ψ^κ separate the energy into independent penalties on shearing and volume change. Here $a = -\frac{1}{d}$, d is the problem dimension, $J = \det(\boldsymbol{F})$, μ is the shearing modulus, and κ is the bulk modulus. The Kirchhoff stress associated with this model is

$$\boldsymbol{\tau} = \mu J^{-\frac{2}{d}} \mathrm{dev}(\mathbf{b}) + J\Psi^{\kappa\prime}(J)\boldsymbol{I}, \tag{10}$$

where $\boldsymbol{b} = \boldsymbol{F}\boldsymbol{F}^T$ is the left Cauchy-Green strain, and $\mathrm{dev}(\boldsymbol{A}) = \boldsymbol{A} - \frac{\mathrm{tr}(\boldsymbol{A})}{d}\boldsymbol{I}$ is the deviatoric part of any tensor $\boldsymbol{A}$. See [Wolper et al. 2019] for the stress derivations for implicit integration.

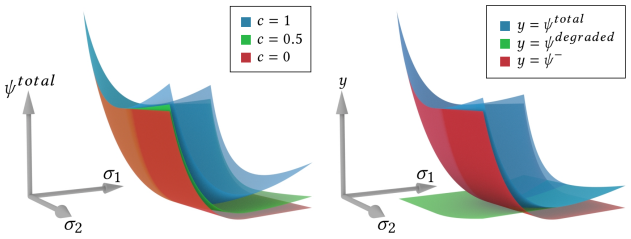

Fig. 14. **Split Energy Density.** (Left) Total energy, Ψ^E, plotted for three damage values; note the overlapping energies when principal stretches σ_1 and σ_2 are below 1. (Right) Decomposition of Ψ^E into components, $\Psi^{\text{degraded}} = g(c)\Psi^+$ and Ψ^-.

The use of Ψ^μ and Ψ^κ further allows the decomposition of Ψ^E into tensile (Ψ^+) and compressive (Ψ^-) parts [Amor et al. 2009]:

$$\Psi^+ = \begin{cases} \Psi^\mu(J^a\boldsymbol{F}) + \Psi^\kappa(\boldsymbol{F}) & J \geq 1 \\ \Psi^\mu(J^a\boldsymbol{F}) & J < 1 \end{cases}, \quad \Psi^- = \begin{cases} 0 & J \geq 1 \\ \Psi^\kappa(\boldsymbol{F}) & J < 1 \end{cases}.$$

This decomposition is then combined with Eqn. (3) to get the final damaged $\hat{\Psi}$. We visualize this split energy density scheme in Fig. 14 for different values of damage and with the components separated to show the role each plays in the total energy. Furthermore, we find that the split scheme we adopt is visually comparable to both the fixed corotated and Neo-Hookean energy densities (see Fig. 15).

6 PLASTICITY

We present a method to form an approximate analytic solution of plasticity treatment for a wide range of plasticity models whose yield surfaces, denoted y, can be expressed as a function of the Kirchhoff stress $\boldsymbol{\tau}$. This treatment corresponds to performing a plastic projection to fulfill $y(\boldsymbol{\tau}) \leq 0$. We will first explain the general framework, and then introduce a novel Non-Associated Cam-Clay model (NACC) with a new strain hardening scheme that is able to capture many fracture behaviors. Our method also renders analytic solutions to the von Mises and Drucker-Prager plasticity models.

6.1 Generalized Non-associated Return Mapping

We adopt the multiplicative decomposition of $\boldsymbol{F}$ into elastic and plastic parts $\boldsymbol{F} = \boldsymbol{F}^E\boldsymbol{F}^P$, where only $\boldsymbol{F}^E$ contributes to the elastic potential energy. Introducing $\boldsymbol{b}^E = \boldsymbol{F}^E\boldsymbol{F}^{E^T}$ and $\mathbf{C}^P = \boldsymbol{F}^{P^T}\boldsymbol{F}^P$, plastic flow becomes a rule on the evolution of $\boldsymbol{b}^E$ [Klár et al. 2016]:

$$\frac{D\boldsymbol{b}^E}{Dt} = \frac{D\boldsymbol{F}}{Dt}\mathbf{C}^{P^{-1}}\boldsymbol{F}^T + \boldsymbol{F}\mathbf{C}^{P^{-1}}\frac{D\boldsymbol{F}^T}{Dt} + \boldsymbol{F}\frac{D\mathbf{C}^{P^{-1}}}{Dt}\boldsymbol{F}^T. \quad (11)$$

Operator splitting can be applied to the integration of $\boldsymbol{b}^E$ [Simo 1988]. The first step only considers the first two terms, which correspond to a "trial" elastic step going from $\boldsymbol{b}^{E,n}$ to $\boldsymbol{b}^{E,\text{tr}}$. In practice, this can be done by evolving the deformation gradient from t^n to t^{n+1} assuming no plasticity. After that, we integrate from $\boldsymbol{b}^{E,\text{tr}}$ to $\boldsymbol{b}^{E,n+1}$ by choosing a proper projection direction $\boldsymbol{G}$, where $\boldsymbol{G} = \frac{\partial y}{\partial \boldsymbol{\tau}}$ for associated plasticity, and $\boldsymbol{G} = \text{dev}(\frac{\partial y}{\partial \boldsymbol{\tau}})$ for non-associated plasticity. This projects the trial state back into the yield surface. The

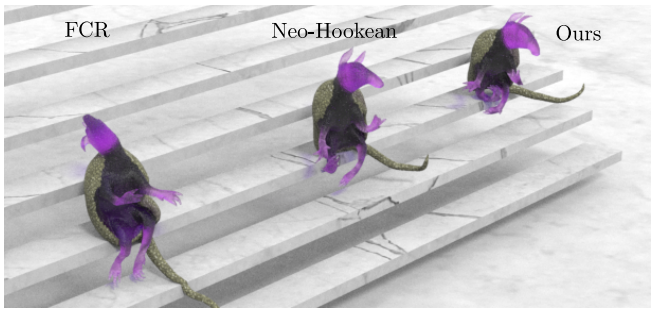

Fig. 15. **Armadillo Fall.** Three realistic jello armadillos fell down the stairs using three different energy densities, demonstrating the comparable elastic behavior of the split energy density scheme we adopt.

ODE to be integrated from $\boldsymbol{b}^{E,\text{tr}}$ to $\boldsymbol{b}^{E,n+1}$ is then

$$\frac{D\boldsymbol{b}^E}{Dt} = -2\gamma\boldsymbol{G}\boldsymbol{b}^E, \quad (12)$$

where γ is an unknown scalar. Klár et al. [2016] solve the ODE using an exponential integrator and their method gives an analytic solution for the Drucker-Prager plasticity model under their choice of elasticity. Unfortunately, applying their approach to more complex plasticity models such as the Cohesive Cam-Clay model would result in a local Newton solve per particle [Gaume et al. 2018], which largely affects the efficiency and ease of implementation. Inspired by the treatment of von Mises plasticity by Borden et al. [2016], we use a backward Euler solver for the ODE, and seek to show the existence of an approximate analytic solution for a wide range of general yield surfaces. We also focus our study on non-associated plasticity due to the geometric correctness of its enforcement of volume preserving plastic deformation [Wolper et al. 2019]. With $\delta\gamma = \gamma\Delta t$, the backward Euler discretization of Eqn. (12) is:

$$\boldsymbol{b}^{E,n+1} - \boldsymbol{b}^{E,\text{tr}} = -2\delta\gamma\boldsymbol{G}(\boldsymbol{b}^{E,n+1})\boldsymbol{b}^{E,n+1}. \quad (13)$$

As proved in [Klár et al. 2016], for isotropic materials, it becomes much more convenient to solve Eqn. (13) in the diagonal space obtained from the singular value decomposition of the deformation gradient. Similar to the elastic potential energy which can be rewritten as $\Psi(\boldsymbol{F}) = \Psi(\hat{\boldsymbol{F}})$ for isotropic materials, the yield surface can also be re-expressed as $y(\boldsymbol{\tau}) = y(\hat{\boldsymbol{\tau}})$. Notice we use $\hat{\boldsymbol{A}}$ to denote the corresponding quantities in the diagonal space for any tensor $\boldsymbol{A}$. We can further decompose $\hat{\boldsymbol{\tau}}$ into two parts: $\hat{\boldsymbol{\tau}} = \hat{\boldsymbol{s}} + p\mathbf{1}$, where $\mathbf{1}$ represents the all-ones vector, $\hat{\boldsymbol{s}} = \text{dev}(\hat{\boldsymbol{\tau}})$ is the deviatoric portion and $p = -\frac{1}{d}\text{tr}(\hat{\boldsymbol{\tau}})$ is the pressure portion. As their names indicate, $\hat{\boldsymbol{s}}$ essentially encodes the shearing information while p encodes the dilation information. Although in 3D $\hat{\boldsymbol{s}}$ seems to have three degrees of freedom, it can be deduced from its definition that $\hat{\boldsymbol{s}}$ must be trace free (or the sum of the three diagonal space entries is zero). Most common yield surfaces have symmetry w.r.t the pressure axis, further removing another degree of freedom. As a result, we can simply use a scale of its magnitude $q = \sqrt{\frac{6-d}{2}}||\hat{\boldsymbol{s}}||$ to describe the yield surface as $y(p, q) = 0$.

With our hyperelasticity model defined in Eqn. (10), it can be shown that for stiff materials (which is indeed the case for most

ductile materials like metal), $\hat{\boldsymbol{s}}^{n+1}$ and $\hat{\boldsymbol{s}}^{\text{tr}}$ are approximately in the same direction. For a non-associated flow rule, we further have $p^{n+1} = p^{\text{tr}}$. Thus, in our framework, the only essential unknown for plastic projection is q^{n+1} (greatly simplifies return mapping).

In the following subsections, we apply our general return mapping algorithm to different plasticity models, including Cam-Clay, von Mises and Drucker-Prager. Each of them defines a specific form for $y(p, q)$. For brevity, we omit the discussion of cases when plasticity projection is not required, i.e. the trial state is already inside the yield surface. We refer to [Wolper et al. 2019] for more details.

6.2 Non-Associated Cam-Clay (NACC)

In 1968, Roscoe et al. [1968] proposed the Modified Cam-Clay yield surface to model clay and soil plasticity; though this model is much used today, the model lacks cohesion and thus has no stress under tension (useful for dry, granular materials). Gaume et al. [2018] augmented MCC by adding cohesive forces to form the Cohesive Cam-Clay (CCC) model which is shown to produce physically accurate anti-crack propagation in snow. Inspired by this successful softening based fracture behavior, we seek to expand CCC by adopting a non-associated flow rule that preserves volume during plasticity projection to generalize this model to other materials.

In general, an associated flow rule enforces that the plastic strain rate is parallel to the gradient of the yield surface; conversely, any non-orthogonal plastic flow rule can be said to be non-associated. Both MCC and CCC are associated flow rules and neither are volume preserving; thus, we design a non-associated flow rule inspired by CCC to enforce isochoric plastic behavior. Here we present details for NACC (derivations and pseudocode in [Wolper et al. 2019]).

6.2.1 NACC Yield Surface. We begin with the CCC yield surface used by Gaume et al. [2018]:

$$y(p, q) = q^2(1 + 2\beta) + M^2(p + \beta p_0)(p - p_0).$$

where β is the cohesion coefficient, M controls the friction, and p_0 relates to the hardening behavior intrinsic to different materials. Furthermore, $p_0 = K\sinh(\xi max(-\alpha, 0))$ where $K = \frac{2}{3}\mu + \lambda$ is the bulk modulus, ξ is the hardening factor, and the variable α is used to track hardening (see Fig. 16 to see parameter effects). Note we use α_0 to denote the initial input state of α before it has been updated.

We expand on CCC [Gaume et al. 2018] by replacing their associated flow rule with our non-associated flow rule that ensures the plasticity projections preserve volume, $J^{P,n+1} = J^{P,\text{tr}}$, avoiding the volume gain inherent to CCC (see Fig. 17). As discussed in §6.1, our plasticity projection also leaves the pressure unchanged giving the following relationships: $J^{E,n+1} = J^{E,\text{tr}}$ and $p^{n+1} = p^{\text{tr}}$. With this we may rewrite the yield surface as follows:

$$y(p^{\text{tr}}, q) = q^2(1 + 2\beta) + M^2(p^{\text{tr}} + \beta p_0)(p^{\text{tr}} - p_0) = 0. \quad (14)$$

Eqn. (14) gives an analytic way to compute the desired q using p^{tr}; however, this equation does not have a solution for q when the trial pressure renders the second term negative. This discontinuity requires that our return mapping be broken down into cases.

6.2.2 NACC Return Mapping. Once p^{tr} is computed from $\boldsymbol{b}^{E,tr}$, we compare it with the known minimum and maximum p values that lie on the yield surface: $p_{\text{max}} = p_0$ and $p_{\text{min}} = -\beta p_0$. Our return mapping is therefore broken down into three distinct cases based on the value of p^{tr} in relation to p_{max} and p_{min}: *Case 1* is when $p^{\text{tr}} > p_0$, *Case 2* is when $p^{\text{tr}} < -\beta p_0$, and *Case 3* is when p^{tr} is in the valid range of yield surface values, $-\beta p_0 < p^{\text{tr}} < p_0$.

In the first two cases p^{tr} is found to be entirely outside the range of valid p values within the yield surface (rendering Eqn. (14) unsolvable), and as such we must project to the tips of the ellipsoid. This projection is as simple as setting $p^{n+1} = p_0$ in case 1 or $p^{n+1} = -\beta p_0$ in case 2 and $q = 0$ in both cases; we can then compute $J^{E,n+1} = \sqrt{\frac{-2p^{n+1}}{\kappa} + 1}$ and use the result to reconstruct the principal stretch with $\Sigma^{E,n+1} = (J^{E,n+1})^{\frac{1}{d}}\boldsymbol{I}$. Conversely, in case 3, Eqn. (14) is trivially solvable with two solutions; however, since q represents a magnitude, only the positive solution is valid.

6.2.3 Fracture-Friendly Hardening. In order to track hardening we update the volumetric and shear plastic deformation with a hardening parameter α. For the first two cases, dilational motion is dominant and α encodes changes in $\log(J^P)$; this is achieved by using the relationship between the decomposed deformation gradient before and after the second ODE solve: $F = F^{E,\text{tr}}F^{P,n} = F^{E,n+1}F^{P,n+1}$. Through taking the determinant of both sides, we find that in case 1 and 2, the change in α can be simply computed as $\log(\frac{J^{E,\text{tr}}}{J^{E,n+1}})$.

However, in case 3 we have plastic flow enduring pure shearing and our non-associated flow rule does not change J^P, making this simple hardening inapplicable. Instead, we propose a novel approach that allows volume-preserving fractures to occur under pure shearing while still updating the yield surface with appropriate

Fig. 16. **NACC Parameters.** The NACC parameters α and β are shown to strongly control fracture behavior, giving significant artistic control.

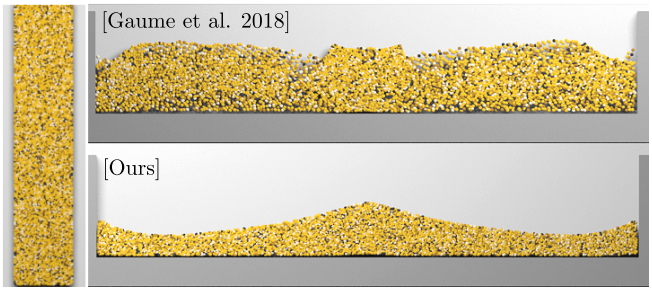

Fig. 17. **Volume Gain.** We compare a sand column collapse using CCC and NACC (both with hardening disabled) to demonstrate the volume gain improvement attained through adopting a non-associated flow rule.

hardening. We observe that on the larger p side of the ellipsoid we need to enforce material hardening, and on the other side, material softening (allowing natural fracture). Therefore, we define the intersection point, $(p^\times, q^\times)$, to be the common point shared both by the yield surface ellipsoid and by the line connecting the trial state, $(p^{\text{tr}}, q^{\text{tr}})$, and the ellipsoid center, (p^c, q^c), (an illustrative figure is provided in [Wolper et al. 2019]). Specifically, this line is:

$$(p^\times, q^\times) = (p^c, q^c) + l\frac{(p^c, q^c) - (p^{\text{tr}}, q^{\text{tr}})}{||(p^c, q^c) - (p^{\text{tr}}, q^{\text{tr}})||},$$

where l is a scalar deciding where the point $(p^\times, q^\times)$ resides. Further, since the intersection point is also on the yield surface, we can get $q^{\times 2}(1 + 2\beta) + M^2(p^\times + \beta p_0)(p^\times - p_0) = 0$. We combine these two equations to get a quadratic equation: $Al^2 + Bl + C = 0$ with A, B and C being some constants, allowing us to solve for two solutions to l. We choose the l such that $(p^{\text{tr}} - p^c)(p^\times - p^c) > 0$, i.e. $p^\times$ is on the same side of the center as p^{tr}. Choosing the correct side of the ellipsoid captures the damage caused by shearing, and triggers more intensive softening when the shearing happens quickly. From $p^\times$ we can compute $J^{E,\times}$, which is employed to perform the update to α similar to the first two cases as $\log(\frac{J^{E,\text{tr}}}{J^{E,\times}})$.

We introduce the variable α due to this hardening case because α is no longer the true $\log(J^P)$, just the hardening state we track. Further, note that NACC plasticity causes fracture to occur strictly through material softening and, as such, does not fully reduce tensile stress to zero, but instead allows fracture to occur at high stress while obeying plasticity rules and flow as defined.

6.3 Non-associated von Mises and Drucker-Prager

We demonstrate the great versatility of our general return mapping approach by presenting straightforward reformulations of both the von Mises (VM) and Drucker-Prager (DP) yield criteria. Here we concisely present the key differences of the two surfaces. In the case of VM, the yield surface is defined by $y(p^{\text{tr}}, q) = \sqrt{\frac{2}{6-d}}(q - \boldsymbol{\tau}_y)$ where $\boldsymbol{\tau}_y$ is the yield strength. Thus, q^{n+1} is simply the yield strength. In Fig. 18 we demonstrate the efficacy of our VM general return mapping by pairing phase-field damage with our non-associated VM plasticity. Similarly, DP has a specific yield surface defined as $y(p^{\text{tr}}, q) = -dc_f p^{\text{tr}} + \sqrt{\frac{2}{6-d}}q - c_c$. We demonstrate in Fig. 19 the visually indistinguishable appearance of our non-associated DP plasticity compared to [Klár et al. 2016] for a sand column collapse.

Fig. 18. **Fence Smash.** A getaway car smashes through a metal fence leaving intricate ductile debris and demonstrating the results attainable through pairing von Mises plasticity with PFF-MPM ($\boldsymbol{\tau}_y = 35$).

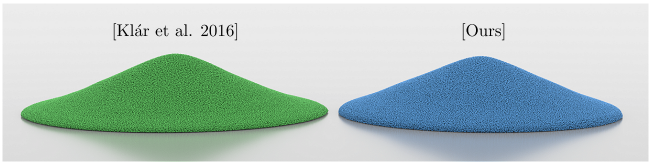

Fig. 19. **Column Collapse.** Our Drucker-Prager plasticity paired with our split energy density gives nearly identical visual results when compared with the exponential return mapping of Klár et al. [2016].

6.4 Ductile Fracture

Combining phase-field evolution and plasticity models allows us to model various ductile fracture phenomena. However, note that Choo and Sun [2018] recently highlighted a key implementation detail: an "effective stress" (the stress *without* degradation) should be used to evaluate the yield function and perform the return mapping. This choice comes from the hypothesis of strain equivalence in damage mechanics that states the strain associated with a damaged state under the applied stress is equivalent to the strain associated with its undamaged state under the effective stress. Fortunately, this greatly simplifies the generalization of PFF-MPM, since incorporating an existing plasticity model into our framework does not require any modification to the existing return mapping implementation.

7 RESULTS

We present a breadth of demos to demonstrate the robust fracture achievable with NACC and PFF. All demos were run on an Intel Core i7-8700K CPU with 12 threads at 3.70 GHz, and all timings and material parameters are organized in Table 2. We did not note any significant qualitative or performance differences when using implicit or explicit integration for these demos, but we list these for completeness. All code will be open-sourced on authors' homepages.

We first demonstrate the diversity of fracture attainable with NACC alone. We explore the effect of the parameters in Fig. 16 with a pumpkin smash, demonstrating the rich artistic control. Then we present the same simulation in Fig. 9 with a visualization of α to represent crack growth. In Fig. 8 we show brittle fracture of a crab-shaped candy alongside a material space crack visual. We further demonstrate brittle behavior in Fig. 3 with a cookie smash by using a stiffer material for the cookie and a softer one for the cream, achieving complex debris. Finally, we present in Fig. 5 a watermelon smash (again with a stiffer material for the rind), illustrating the robust organic material fracture possible with NACC. Note that these demos do not utilize PFF-MPM. Furthermore, we performed a performance test by smashing a pumpkin and found that the plasticity kernel of CCC took 111.61 seconds while NACC took 47.96 seconds, achieving more than 2× speedup.

We now present various results using PFF-MPM to show the breadth of fracture achievable. We exploreits rich parameters in Fig. 10. The comparison between values of $\mathcal{G}$ illustrates the sensitivity of the energy release rate and the achievable fracture effects. Similarly, various settings of the fracture mobility constant M_c show the (less dramatic) effect fracture speed has on the ensuing fracture patterns. We further present experiments inspired by standard mechanics tests to show the advantages of our non-local CDM over

Table 2. **Parameters and Timings.** Seconds per frame is provided as an average with all demos run on an Intel i7-8700K CPU with 12 threads at 3.70 GHz. All parameters are reported in standard CGS units.

Example	Scheme	s/frame	Δt_{frame}	Δx	Δt_{step}	N	ρ	E	ν	PFF-($\mathcal{G}$, M_c)	NACC-(α_0, β, ξ, M)
(Fig. 3) Cookie	explicit	634.5	1/48	4×10^{-3}	1.15×10^{-5}	1.67M	2	2×10^4/1000	0.4/0.35	-	(-0.01/-0.03, 0.5/1, 0.8/1, 2.36)
(Fig. 9) Pumpkin	explicit	176.7	1/24	7×10^{-3}	5.64×10^{-5}	1.02M	2	2000	0.39	-	(-0.04, 2, 3, 2.36)
(Fig. 5) Melon	explicit	313.4	1/24	7×10^{-3}	5.44×10^{-5}	1.75M	2	2000/1000	0.4/0.3	-	(-0.01/-0.03, 2/1, 3, 2.36)
(Fig. 8) Crab	explicit	96.8	1/120	4×10^{-3}	1.71×10^{-5}	918K	2	2×10^4	0.35	-	(-0.01, 0.5, 1, 2.36)
(Fig. 7) Octocat	implicit	17.6	1/24	3.91×10^{-3}	2×10^{-3}	690K	2	20	0.4	$(3.43 \times 10^{-2}, 10)$	-
(Fig. 4) Bar Twist	explicit	548.6	1/24	1×10^{-2}	1×10^{-3}	7.79M	2	50	0.4	$(3.79 \times 10^{-2}, 1)$	-
(Fig. 18) Fence	implicit	175.2	1/120	6×10^{-3}	8×10^{-3}	1.45M	2	2×10^4	0.4	$(1.35 \times 10^{-2}, 15)$	-
(Fig. 2) T-Rex	implicit	538.8	1/30	1.2×10^{-2}	1×10^{-4}	1.43M	0.1	20	0.4	$(3.43 \times 10^{-2}, 15)$	-
(Fig. 1) Bread	explicit	331.7	1/480	2.82×10^{-3}	3.82×10^{-5}	11.5M	2	500	0.4	$(3.79 \times 10^{-1}, 1)$	-
(Fig. 6) Stretch	explicit	118.3	1/120	5×10^{-3}	3×10^{-4}	8.27M	2	50	0.4	$(3.79 \times 10^{-2}, 1)$	-

local CDM; we find that PFF-MPM not only more adequately captures all modes of fracture, but also produces resolution invariant crack propagation (see [Wolper et al. 2019]).

We compare PFF-MPM against numerical fracture in Fig. 2, where a jello T-rex is shot with a bullet; the fracture path is visibly formed when PFF is used, and conversely, numerical fracture produces unrealistic behavior. Similarly, we perform the same comparison using a jello bar twist in Fig. 4 to further show the importance of the phase-field. In Fig. 6, we tear the limbs off the armadillo and visualize the phase-field. To further illustrate the material space phase-field propagation, we show in Fig. 7 two colliding elastic "octocats," each with fragile tendril-like arms prone to fracture. We also pair our phase-field with von Mises plasticity ($\tau_y = 35$) to perform a metal fracture simulation in Fig. 18 where a getaway car smashes through a metal fence, leaving an intricate hole with plastically deformed edges and debris. Finally, in Fig. 1 we illustrate the hyper-realistic fracture effects attainable through using PFF-MPM to capture the intricate behavior intrinsic to tearing fresh bread. In Fig. 20 we present a timing breakdown for a single substep of the implicit jello T-rex in PFF-MPM; the proportionally-small compute time added by our phase-field augmentation highlights that PFF-MPM is an extremely efficient augmentation of traditional MPM that adds comparatively little overhead to the existing computations.

Note that in many of our demos pieces of the material separate and come back together without actually reconnecting; however, at times there appears to be a stickiness to this interaction. We note that this is not intrinsic to the augmentations that make up CD-MPM, but actually this interpolation induced stickiness is unfortunately a known limitation of the MPM algorithm itself.

8 LIMITATIONS AND FUTURE WORK

Although our two approaches are robust and resolve intricate cracks with extremely high visual fidelity, CD-MPM has limitations related to rendering and parameter tuning. Specifically, MPM simulations are often rendered using meshed particles followed by smoothing (we used OpenVDB [Museth et al. 2013]); however, rendering debris is difficult due to the delicate balance between surface smoothness and sharpness. Smoothing too much removes the intricate crack patterns, but smoothing too little leaves the surface undesirably textured. Due to these difficulties, CD-MPM is an opportune target for augmentation through surface tracking and reconstruction techniques, such as the level-set method of Bhatacharya et al. [2011] or other triangle mesh approaches [Da et al. 2014; Yu et al. 2012]. Similarly, to achieve detailed cracks, the grid resolution must be sufficiently high; however, this is mitigated by the length scale parameter l_0, since we set it based on grid resolution. Fortunately, we found that phase-field crack propagation speed is resolution invariant, while for local CDM it is not [Wolper et al. 2019].

While both PFF-MPM and NACC have rich artistic control capabilities due to their many parameters, tuning does have a notable learning curve. We show the breadth of effects possible simply through changing parameters, but the parameters themselves are admittedly esoteric and at first difficult to tune due to the high sensitivity of parameters like $\mathcal{G}$. We believe the rich control is worth the difficulty, but it is clear that a more intuitive parameter formulation would much better assist artists and practitioners alike. Furthermore, there are some visual effects that are still hard to capture (such as controlling/predicting the amount of debris).

CD-MPM provides a new generalized return mapping that enables myriad material effects and, as such, presents a unique and robust framework to explore other fracture effects such as brittle and anisotropic fracture. We explored brittle fracture and found that PFF-MPM somewhat struggles to produce fast and rigid shatter effects; however, we did find some success, specifically with our

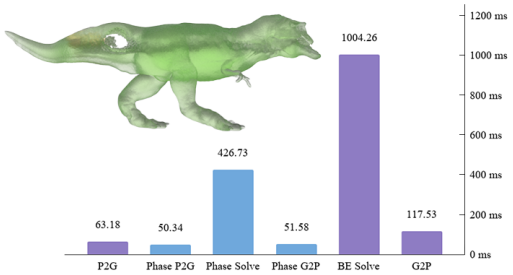

Fig. 20. **PFF-MPM Substep Timing Breakdown.** Decomposing a single substep of PFF-MPM into its subroutines shows the comparatively low compute time our phase computations (blue) add to traditional MPM (purple). Timing was performed on an implicit demo (see Fig. 2) to show that the phase solve takes less than half the time of the Backward Euler solve.

NACC model (see Fig. 8). Conversely, anisotropic fracture requires further modeling of grain patterns and their effect on the fracture of materials such as wood, biological tissues, and crystal.

As discussed, the parameters within CD-MPM could be expanded to be more intuitive, and the development of reformulated parameters may assist with enabling such an interface. Furthermore, the robust behaviors producible by changing the sensitive $\mathcal{G}$ parameter show great promise for artistically controllable fracture patterns through clever initializations of $\mathcal{G}$ (for example using Voronoi tessellation). Early exploration of alternative initializations produced promising results. Finally, some orthogonal extensions: a rigorous study of the convergence of staggered iterations, a thorough investigation of the effects possible through coupling PFF and NACC, and the incorporation of particle resampling (such as that of Yue et al. [2015]) to mitigate the undesirable effects of undersampled regions. This last extension is noteworthy due to the visual similarity of numerical fracture and the true fracture behavior we desire.

ACKNOWLEDGMENTS

We would like to thank Matt Alexander for bringing Figs. 12 and 13 to life, Johan Gaume for useful discussions, Hannah Bollar for narrating the video, and the anonymous reviewers for their valuable comments. This work was supported in part by NSF Grants IIS-1755544 and CCF-1813624, a gift from Harlan Stone, a gift from Adobe Inc., NVIDIA GPU grants, and Houdini licenses from SideFX.

REFERENCES

S. M. Allen and J. W. Cahn. 1972. Ground state structures in ordered binary alloys with second neighbor interactions. *Acta Metallurgica* 20, 3 (1972), 423–433.

M. Ambati, R. Kruse, and L. De Lorenzis. 2016. A phase-field model for ductile fracture at finite strains and its experimental verification. *Comp. Mech.* 57, 1 (2016), 149–167.

H. Amor, J.-J. Marigo, and C. Maurini. 2009. Regularized formulation of the variational brittle fracture with unilateral contact: Numerical experiments. *J. of the Mech. and Phys. of Solids* 57, 8 (2009), 1209–1229.

K. Aoki, N. H. Dong, T. Kaneko, and S. Kuriyama. 2004. Physically Based Simulation of Cracks on Drying 3D Solids. In *Proc. of the Comp. Graph. Int.* 357–364.

I. S. Aranson, V. A. Kalatsky, and V. M. Vinokur. 2000. Continuum field description of crack propagation. *Physical Review Letters* 85, 1 (2000), 118–121.

Z. Bao, J. M. Hong, J. Teran, and R. Fedkiw. 2007. Fracturing Rigid Materials. *IEEE Trans. on Vis. and Comp. Graph.* 13, 2 (2007), 370–378.

G. I. Barenblatt. 1962. The Mathematical Theory of Equilibrium Cracks in Brittle Fracture. Advances in Applied Mechanics, Vol. 7. 55 – 129.

T. Belytschko and T. Black. 1999. Elastic crack growth in finite elements with minimal remeshing. *Int. J. for Num. Meth. in Eng.* 45, 5 (1999), 601–620.

T. Belytschko, D. Organ, and Y. Krongauz. 1995. A coupled finite element-element-free Galerkin method. *Comp. Mech.* 17, 3 (1995), 186–195.

H. Bhatacharya, Y. Gao, and A. Bargteil. 2011. A Level-set Method for Skinning Animated Particle Data. In *Symp. Comp. Anim.* 17–24.

M. J. Borden, T. J.R. Hughes, C. M. Landis, A. Anvari, and I. J. Lee. 2016. A phase-field formulation for fracture in ductile materials: Finite deformation balance law derivation, plastic degradation, and stress triaxiality effects. *Comp. Meth. in Applied Mech. and Eng.* 312 (2016), 130–166.

M. J. Borden, C. V. Verhoosel, M. A. Scott, T. JR. Hughes, and C. M. Landis. 2012. A phase-field description of dynamic brittle fracture. *Comp. Meth. in Applied Mech. and Eng.* 217 (2012), 77–95.

S. Bouaziz, S. Martin, T. Liu, L. Kavan, and M. Pauly. 2014. Projective Dynamics: Fusing Constraint Projections for Fast Simulation. *ACM Trans. Graph.* 33, 4 (2014), 154:1–154:11.

B. Bourdin, G. A. Francfort, and J-J. Marigo. 2000. Numerical experiments in revisited brittle fracture. *J. of the Mech. and Phys. of Solids* 48, 4 (2000), 797 – 826.

B. Bourdin, G. A. Francfort, and J.-J. Marigo. 2008. The variational approach to fracture. *Journal of elasticity* 91, 1-3 (2008), 5–148.

J. Brackbill and H. Ruppel. 1986. FLIP: A method for adaptively zoned, Particle-In-Cell calculations of fluid flows in two dimensions. *J Comp Phys* 65 (1986), 314–343.

O. Busaryev, T. K. Dey, and H. Wang. 2013. Adaptive Fracture Simulation of Multi-layered Thin Plates. *ACM Trans. Graph.* 32, 4, Article 52 (2013), 6 pages.

J. W. Cahn and J. E. Hilliard. 1958. Free energy of a nonuniform system. I. interfacial free energy. *The Journal of Chemical Physics* 28, 2 (1958), 258–267.

M. Cervera and M. Chiumenti. 2006. Mesh objective tensile cracking via a local continuum damage model and a crack tracking technique. *Comp. Meth. in Applied Mech. and Eng.* 196, 1-3 (2006), 304–320.

F. Chen, C. Wang, B. Xie, and H. Qin. 2013. Flexible and rapid animation of brittle fracture using the smoothed particle hydrodynamics formulation. *Computer Animation and Virtual Worlds* 24, 3-4 (2013), 215–224.

Z. Chen, M. Yao, R. Feng, and H. Wang. 2014. Physics-inspired Adaptive Fracture Refinement. *ACM Trans. Graph.* 33, 4, Article 113 (2014), 7 pages.

J. Choo and W. C. Sun. 2018. Coupled phase-field and plasticity modeling of geological materials: From brittle fracture to ductile flow. *Comp. Meth. in Applied Mech. and Eng.* 330 (2018), 1–32.

F. Da, C. Batty, and E. Grinspun. 2014. Multimaterial Mesh-based Surface Tracking. *ACM Trans. Graph.* 33, 4, Article 112 (2014), 11 pages.

F. Da, D. Hahn, C. Batty, C. Wojtan, and E. Grinspun. 2016. Surface-only Liquids. *ACM Trans. Graph.* 35, 4, Article 78 (2016), 12 pages.

G. Daviet and F. Bertails-Descoubes. 2016. A semi-implicit material point method for the continuum simulation of granular materials. *ACM Trans. Graph.* 35, 4 (2016).

Y. (R.) Fei, C. Batty, E. Grinspun, and C. Zheng. 2018. A Multi-scale Model for Simulating Liquid-fabric Interactions. *ACM Trans. Graph.* 37, 4 (2018), 51:1–51:16.

G. A. Francfort and J.-J. Marigo. 1998. Revisiting brittle fracture as an energy minimization problem. *J. of the Mech. and Phys. of Solids* 46, 8 (1998), 1319–1342.

M. Gao, A. Pradhana, X. Han, Q. Guo, G. Kot, E. Sifakis, and C. Jiang. 2018a. Animating fluid sediment mixture in particle-laden flows. *ACM Trans. Graph.* 37, 4 (2018), 149.

M. Gao, X. Wang, K. Wu, A. Pradhana, E. Sifakis, C. Yuksel, and C. Jiang. 2018b. GPU Optimization of Material Point Methods. *ACM Trans. Graph.* 37, 6, Article 254 (2018), 12 pages.

J. Gaume, T. Gast, J. Teran, A. van Herwijnen, and C. Jiang. 2018. Dynamic anticrack propagation in snow. *Nature communications* 9, 1 (2018), 3047.

L. Glondu, M. Marchal, and G. Dumont. 2013. Real-Time Simulation of Brittle Fracture Using Modal Analysis. *IEEE Trans. on Vis. and Comp. Graph.* 19, 2 (2013), 201–209.

L. Glondu, S. C. Schvartzman, M. Marchal, G. Dumont, and M. A. Otaduy. 2014. Fast Collision Detection for Fracturing Rigid Bodies. *IEEE Trans. on Vis. and Comp. Graph.* 20, 1 (2014), 30–41.

P. Grassl and M. Jirásek. 2004. On mesh bias of local damage models for concrete. (2004).

A. A. Griffith and M. Eng. 1921. VI. The phenomena of rupture and flow in solids. *Phil. Trans. R. Soc. Lond. A* 221, 582-593 (1921), 163–198.

Q. Guo, X. Han, C. Fu, T. Gast, R. Tamstorf, and J. Teran. 2018. A material point method for thin shells with frictional contact. *ACM Trans. Graph.* 37, 4 (2018), 147.

D. Hahn and C. Wojtan. 2015. High-resolution brittle fracture simulation with boundary elements. *ACM Trans. Graph.* 34, 4, Article 151 (2015), 12 pages.

D. Hahn and C. Wojtan. 2016. Fast approximations for boundary element based brittle fracture simulation. *ACM Trans. Graph.* 35, 4, Article 104 (2016), 11 pages.

X. He, H. Wang, and E. Wu. 2018. Projective peridynamics for modeling versatile elastoplastic materials. *IEEE Trans. on Vis. and Comp. Graph.* 24, 9 (2018), 2589–2599.

X. He, H. Wang, F. Zhang, H. Wang, G. Wang, K. Zhou, and E. Wu. 2015. Simulation of fluid mixing with interface control. In *Symp. Comp. Anim.* 129–135.

J. Hegemann, C. Jiang, C. Schroeder, and J. Teran. 2013. A level set method for ductile fracture. In *Proc ACM SIGGRAPH/Eurograp Symp Comp Anim.* 193–201.

K. Hirota, Y. Tanoue, and T. Kaneko. 1998. Generation of crack patterns with a physical model. *The Visual Computer* 14, 3 (1998), 126–137.

K. Hirota, Y. Tanoue, and T. Kaneko. 2000. Simulation of three-dimensional cracks. *The Visual Computer* 16, 7 (2000), 371–378.

M. A. Homel and E. B. Herbold. 2017. Field-gradient partitioning for fracture and frictional contact in the material point method. *Int. J. for Num. Meth. in Eng.* 109, 7 (2017), 1013–1044.

Y. Hu, Y. Fang, Z. Ge, Z. Qu, Y. Zhu, A. Pradhana, and C. Jiang. 2018. A moving least squares material point method with displacement discontinuity and two-way rigid body coupling. *ACM Trans. Graph.* 37, 4 (2018), 150.

G. R. Irwin. 1957. Analysis of Stresses and Strains Near the End of a Crack Traversing a Plate. *J. Appl. Mech.* (1957).

D. L. James and D. K. Pai. 1999. ArtDefo: Accurate real time deformable objects. In *Proc. of the 26th Ann. Conf. on Comp. Graph. and Inter. Tech.* 65–72.

C. Jiang, T. Gast, and J. Teran. 2017. Anisotropic elastoplasticity for cloth, knit and hair frictional contact. *ACM Trans. Graph.* 36, 4 (2017).

C. Jiang, C. Schroeder, A. Selle, J. Teran, and A. Stomakhin. 2015. The affine particle-in-cell method. *ACM Trans. Graph.* 34, 4 (2015), 51:1–51:10.

C. Jiang, C. Schroeder, J. Teran, A. Stomakhin, and A. Selle. 2016. The material point method for simulating continuum materials. In *SIGGRAPH Course.* 24:1–24:52.

B. Jones, A. Martin, J. A. Levine, T. Shinar, and A. W. Bargteil. 2016. Ductile Fracture for Clustered Shape Matching. *Proc. of the ACM SIGGRAPH symp. on Int. 3D graph. and games* (2016).

L. M. Kachanov. 1999. Rupture Time Under Creep Conditions. *Int. J. of Fracture* 97, 1 (1999), 11–18.

P. Kaufmann, S. Martin, M. Botsch, and M. Gross. 2008. Flexible simulation of deformable models using discontinuous Galerkin FEM. In *Symp. Comp. Anim.* 105–116.

T. Kim, M. Henson, and M. C. Lin. 2004. A hybrid algorithm for modeling ice formation. In *Symp. Comp. Anim.* 305–314.

G. Klár, T. Gast, A. Pradhana, C. Fu, C. Schroeder, C. Jiang, and J. Teran. 2016. Drucker-prager elastoplasticity for sand animation. *ACM Trans. Graph.* 35, 4 (2016), 103:1–103:12.

D. Koschier, J. Bender, and N. Thuerey. 2017. Robust eXtended finite elements for complex cutting of deformables. *ACM Trans. Graph.* 36, 4, Article 55 (2017), 13 pages.

L. D. Landau and E. M. Lifshitz. 1971. The classical theory of fields. (1971).

J. A. Levine, A. W. Bargteil, C. Corsi, J. Tessendorf, and R. Geist. 2014. A peridynamic perspective on spring-mass fracture. In *Symp. Comp. Anim.* 47–55.

X. Li, S. Andrews, B. Jones, and A. Bargteil. 2018. Energized rigid body fracture. *Proc. ACM Comput. Graph. Interact. Tech.* 1, 1, Article 9 (2018), 9 pages.

N. Liu, X. He, S. Li, and G. Wang. 2011. Meshless Simulation of Brittle Fracture. *Comput. Animat. Virtual Worlds* 22, 2-3 (2011), 115–124.

T. Liu, A. Bargteil, J. O'Brien, and L. Kavan. 2013. Fast Simulation of Mass-Spring Systems. *ACM Trans. Graph.* 32, 6 (2013), 209:1–7.

T. Liu, S. Bouaziz, and L. Kavan. 2017. Quasi-Newton Methods for Real-Time Simulation of Hyperelastic Materials. *ACM Trans. Graph.* 36, 3, Article 116a (2017).

Y. Y. Lu, T. Belytschko, and M. Tabbara. 1995. Element-free Galerkin method for wave propagation and dynamic fracture. *Comp. Meth. in Applied Mech. and Eng.* 126, 1 (1995), 131 – 153.

C. Miehe, M. Hofacker, and F. Welschinger. 2010a. A phase field model for rate-independent crack propagation: Robust algorithmic implementation based on operator splits. *Comp. Meth. in Applied Mech. and Eng.* 199, 45-48 (2010), 2765–2778.

C. Miehe, L. M. Schänzel, and H. Ulmer. 2015. Phase field modeling of fracture in multi-physics problems. Part I. Balance of crack surface and failure criteria for brittle crack propagation in thermo-elastic solids. *Comp. Meth. in Applied Mech. and Eng.* 294 (2015), 449 – 485.

C. Miehe, F. Welschinger, and M. Hofacker. 2010b. Thermodynamically consistent phase-field models of fracture: Variational principles and multi-field FE implementations. *Int. J. for Num. Meth. in Eng.* 83, 10 (2010), 1273–1311.

N. Mitchell, M. Aanjaneya, R. Setaluri, and E. Sifakis. 2015. Non-manifold level sets: A multivalued implicit surface representation with applications to self-collision processing. *ACM Trans. Graph.* 34, 6 (2015), 247.

N. Moës, J. Dolbow, and T. Belytschko. 1999. A finite element method for crack growth without remeshing. *Int. J. for Num. Meth. in Eng.* 46, 1 (1999), 131–150.

N. Molino, Z. Bao, and R. Fedkiw. 2005. A Virtual Node Algorithm for Changing Mesh Topology During Simulation. In *ACM SIGGRAPH 2005 Courses*. Article 4.

D. Mould. 2005. Image-guided Fracture. In *Proc. of Graphics Interface 2005*. 219–226.

M. Müller and M. Gross. 2004. Interactive Virtual Materials. In *Proc. of Graphics Interface 2004*. 239–246.

M. Müller, R. Keiser, A. Nealen, M. Pauly, M. Gross, and M. Alexa. 2004. Point Based Animation of Elastic, Plastic and Melting Objects. In *Symp. Comp. Anim.* 141–151.

Ken Museth, Jeff Lait, John Johanson, Jeff Budsberg, Ron Henderson, Mihai Alden, Peter Cucka, David Hill, and Andrew Pearce. 2013. OpenVDB: an open-source data structure and toolkit for high-resolution volumes. In *Acm siggraph 2013 courses*. 19.

J. A. Nairn. 2003. Material point method calculations with explicit cracks. *Comp. Mod. in Eng. And Sci.* 4 (2003), 649–663.

R. Narain, M. Overby, and G. E. Brown. 2016. ADMM ⊇ Projective Dynamics: Fast Simulation of General Constitutive Models. In *Symp Comp Anim.* 21–28.

M. Neff and E. Fiume. 1999. A Visual Model for Blast Waves and Fracture. In *Proc. of the 1999 Conference on Graphics Interface '99*. 193–202.

D. Ngo and A. C. Scordelis. 1967. Finite Element Analysis of Reinforced Concrete Beams. *Journal Proceedings* 64. Issue 3.

J. Ning, H. Xu, B. Wu, L. Zeng, S. Li, and Y. Xiong. 2013. Modeling and animation of fracture of heterogeneous materials based on CUDA. *The Visual Computer* 29, 4 (2013), 265–275.

A. Norton, G. Turk, B. Bacon, J. Gerth, and P. Sweeney. 1991. Animation of fracture by physical modeling. *The Visual Computer* 7, 4 (1991), 210–219.

J. F. O'Brien, A. W. Bargteil, and J. K. Hodgins. 2002. Graphical modeling and animation of ductile fracture. *ACM Trans. Graph.* 21, 3 (2002), 291–294.

J. F. O'Brien and J. K. Hodgins. 1999. Graphical Modeling and Animation of Brittle Fracture. In *Proc. of the 26th Ann. Conf. on Comp. Graph. and Inter. Tech.* 137–146.

M. Pauly, R. Keiser, B. Adams, P. Dutré, M. Gross, and L. J Guibas. 2005. Meshless animation of fracturing solids. *ACM Trans. Graph.* 24, 3 (2005), 957–964.

T. Pfaff, R. Narain, J. M. de Joya, and J. F. O'Brien. 2014. Adaptive Tearing and Cracking of Thin Sheets. *ACM Trans. Graph.* 33, 4, Article 110 (2014), 9 pages.

A. Pradhana, T. Gast, G. Klár, C. Fu, J. Teran, C. Jiang, and K. Museth. 2017. Multi-species simulation of porous sand and water mixtures. *ACM Trans. Graph.* 36, 4 (2017).

R. Radovitzky and M. Ortiz. 1999. Error estimation and adaptive meshing in strongly nonlinear dynamic problems. *Comp. Meth. in Applied Mech. and Eng.* 172, 1-4 (1999), 203–240.

D. Ram, T. Gast, C. Jiang, C. Schroeder, A. Stomakhin, J. Teran, and P. Kavehpour. 2015. A material point method for viscoelastic fluids, foams and sponges. In *Symp. Comp. Anim.* 157–163.

Y. R. Rashid. 1968. Ultimate strength analysis of prestressed concrete pressure vessels. *Nuclear Engineering and Design* 7, 4 (1968), 334 – 344.

K. Roscoe and J. Burland. 1968. On the generalised stress-strain behaviour of wet clay. *Eng Plast* (1968), 535–609.

P. Roy, S. P. Deepu, A. Pathrikar, D. Roy, and J. N. Reddy. 2017. Phase field based peridynamics damage model for delamination of composite structures. *Composite Structures* 180 (2017), 972 – 993.

E. Sifakis, K. G. Der, and R. Fedkiw. 2007. Arbitrary cutting of deformable tetrahedralized objects. In *Symp. Comp. Anim.* 73–80.

S. A. Silling. 2000. Reformulation of elasticity theory for discontinuities and long-range forces. *J. of the Mech. and Phys. of Solids* 48, 1 (2000), 175 – 209.

S. A. Silling and E. Askari. 2005. A meshfree method based on the peridynamic model of solid mechanics. *Computers |& Structures* 83, 17 (2005), 1526 – 1535. Advances in Meshfree Methods.

J. C. Simo. 1988. A framework for finite strain elastoplasticity based on maximum plastic dissipation and the multiplicative decomposition: Part I. Continuum formulation. *Comp. Meth. in Applied Mech. and Eng.* 66, 2 (1988), 199–219.

B. Smith, F. de Goes, and T. Kim. 2018. Stable Neo-Hookean Flesh Simulation. *ACM Trans. Graph.* 37, 2 (2018), 12.

A. Stomakhin, R. Howes, C. Schroeder, and J. M. Teran. 2012. Energetically consistent invertible elasticity. In *Symp. Comp. Anim.* 25–32.

A. Stomakhin, C. Schroeder, L. Chai, J. Teran, and A. Selle. 2013. A material point method for snow simulation. *ACM Trans. Graph.* 32, 4 (2013), 102:1–102:10.

A. Stomakhin, C. Schroeder, C. Jiang, L. Chai, J. Teran, and A. Selle. 2014. Augmented MPM for phase-change and varied materials. *ACM Trans. Graph.* 33, 4 (2014), 138:1–138:11.

N. Sukumar, N. Moës, B. Moran, and T. Belytschko. 2000. Extended finite element method for three-dimensional crack modelling. *Int. J. for Num. Meth. in Eng.* 48, 11 (2000), 1549–1570.

N. Sukumar, B. Moran, T. Black, and T. Belytschko. 1997. An element-free Galerkin method for three-dimensional fracture mechanics. *Comp. Mech.* 20, 1 (1997), 170–175.

D. Sulsky, Z. Chen, and H. L. Schreyer. 1994. A particle method for history-dependent materials. *Comp. Meth. in Applied Mech. and Eng.* 118, 1-2 (1994), 179–196.

D. Sulsky, S. Zhou, and H. Schreyer. 1995. Application of a particle-in-cell method to solid mechanics. *Comp Phys Comm* 87, 1 (1995), 236–252.

D. Terzopoulos and K. Fleischer. 1988. Modeling inelastic deformation: viscolelasticity, plasticity, fracture. In *ACM Siggraph Computer Graphics*, Vol. 22. 269–278.

H. Wang and Y. Yang. 2016. Descent Methods for Elastic Body Simulation on the GPU. *ACM Trans. Graph.* 35, 6, Article 212 (2016), 10 pages.

Y. Wang, C. Jiang, C. Schroeder, and J. Teran. 2014. An adaptive virtual node algorithm with robust mesh cutting. In *Symp. Comp. Anim.* 77–85.

M. Wicke, D. Ritchie, B. M. Klingner, S. Burke, J. R. Shewchuk, and J. F. O'Brien. 2010. Dynamic local remeshing for elastoplastic simulation. *ACM Transactions on Graphics* 29, 4 (2010), 49:1–49:11.

J. Wolper, Y. Fang, M. Li, J. Lu, M. Gao, and C. Jiang. 2019. CD-MPM: Continuum damage material point methods for dynamic fracture animation: Supplemental document. *ACM Trans. Graph.* (2019).

J. Wretborn, R. Armiento, and K. Museth. 2017. Animation of crack propagation by means of an extended multi-body solver for the material point method. *Computers & Graphics* 69 (2017), 131 – 139.

J. Y. Wu. 2017. A unified phase-field theory for the mechanics of damage and quasi-brittle failure. *J. of the Mech. and Phys. of Solids* 103 (2017), 72 – 99.

J. Y. Wu. 2018. A geometrically regularized gradient-damage model with energetic equivalence. *Comp. Meth. in Applied Mech. and Eng.* 328 (2018), 612 – 637.

T. Yang, J. Chang, M. C. Lin, R. R. Martin, J. J. Zhang, and S. Hu. 2017. A Unified particle system framework for multi-phase, multi-material visual simulations. *ACM Trans. Graph.* 36, 6, Article 224 (2017), 13 pages.

T. Yang, J. Chang, B. Ren, M. C. Lin, J. J. Zhang, and S. Hu. 2015. Fast multiple-fluid simulation using Helmholtz free energy. *ACM Trans. Graph.* 34, 6, Article 201 (2015), 11 pages.

J. Yu, C. Wojtan, G. Turk, and C. Yap. 2012. Explicit Mesh Surfaces for Particle Based Fluids. *Comput. Graph. Forum* 31, 2pt4 (2012), 815–824.

Y. Yue, B. Smith, C. Batty, C. Zheng, and E. Grinspun. 2015. Continuum foam: a material point method for shear-dependent flows. *ACM Trans. Graph.* 34, 5 (2015), 160:1–160:20.

Y. Yue, B. Smith, P. Y. Chen, M. Chantharayukhonthorn, K. Kamrin, and E. Grinspun. 2018. Hybrid Grains: Adaptive Coupling of Discrete and Continuum Simulations of Granular Media. *ACM Trans. Graph.* 37, 6, Article 283 (2018), 19 pages.

Y. Zhu and R. Bridson. 2005. Animating sand as a fluid. *ACM Trans. Graph.* 24, 3 (2005), 965–972.

Y. Zhu, R. Bridson, and C. Greif. 2015. Simulating rigid body fracture with surface meshes. *ACM Trans. Graph.* 34, 4, Article 150 (2015), 11 pages.